

## **2. Nanoparticle synthesis by spark generation (SG)**

### **2.1 Introduction**

#### **2.1.1 SGs of aerosol monometallic and bimetallic nanoparticles**

Transition metals, due to their conspicuous physicochemical properties, have received considerable attention in many fields [Chen et al., 2003; Mizsei et al., 1998; Sun et al., 2004], and furthermore, the activity and selectivity of the metal particles can be improved by adding the second and/or the third component to the metal [Deki et al., 1999; Lambert et al., 2006; Toshima et al., 1989, 1991 & 1992]. Bimetallic nanoparticles of transition elements constitute an extensive class for size-dependent electrical, chemical, and optical properties that have attracted considerable interest in both academia and industry [Cádenas & Oliva, 2003; Liu et al., 1992; Patel et al., 2005; Tai et al., 2005; Yang et al., 2004]. They are particularly important in the field of catalysis since they often exhibit better properties than their monometallic counterparts [Devarajan et al., 2005; Karski et al., 2005].

There are many investigations of generations of metallic nanoparticles, most generations were performed in liquid solution containing metal ions, reductants and some polymers (protecting agents), so generations have mostly been limited to the colloid particles. Moreover, adding both reducing and protecting agents also highlights the complexity of the generation [Yang et al., 2004]. Recently, investigations have focused much attention to the characters of the “naked” transition metal nanoparticles because a strong metal-polymer interaction such as metal-support interaction (SMSI) is not formed [Harada et al., 2005]. The naked transition metal particles are anticipated as appropriate materials to investigate their surface structures and geometries. Other generations of the metallic nanoparticles, as an applicable method for naked particle generation, were processed by pyrolysis, flame, chemical

vapor deposition, and sputtering. However, these processes demand either high temperatures or a highly vacuumed environment, which are expensive to operate [Lu & Lin, 2000].

Spark generation has been used to generate the particles for a wide range of conductive materials with particles sizes ranging from several nanometers up to ~100  $\mu\text{m}$  in aerosol state [Horvath & Gangl, 2003; Kim & Chang, 2005; Schwyn et al., 1988; Simonin et al., 2007; DeVoe et al., 1989]. Spark generation of particles in aerosol state has some advantages for simple, high purity, easily deliverable, and environmentally friend, however, the characteristics of the spark generation of metallic nanoparticles were rarely reported in the literature.

In this section, the generations of monometallic (palladium (Pd), platinum (Pt), gold (Au) and silver (Ag)) and bimetallic (Pd-Pt, Pd-Au and Pd-Ag) aerosol nanoparticles were reported by homogeneous (spark between two identical material electrodes) and heterogeneous (spark between two different material electrodes) spark generation sets, respectively. Size distribution, generation rate, morphology, and structure of the obtained particles were characterized by scanning mobility particle sizer (SMPS), SEM, EDX, TEM, ICP-AES, and XRD methods. Finally, mechanisms for spark generations of the monometallic and bimetallic particles were proposed.

### **2.1.2 SGs of aerosol carbon nanoparticles**

Even though conventional activated carbon has been widely used for removal of VOC, problems associated with its short and unpredictable life spans need to be solved. The present study first introduces an idea of removing BTX gas in a controllable way through carbon aerosol particles produced by a spark generator made in a laboratory. A commercially available spark generator developed by Helsper et al. (1999), Palas GFG 1000, has recently been used for production of the heterogeneous chemistry of reactive gases [Kamm et al., 1999],

and has been used for production of the role of adsorbed water in reactivity [Kalberer et al., 1999; Kuznetsov et al., 2003]. However, there have been no published studies of VOC gas removal by carbon airborne particles generated by any type of spark generator.

### **2.1.3 SGs of aerosol carbon-encapsulated metal nanoparticles (CEMNs)**

Nanocrystalline metal particles have the disadvantage of being prone to rapid environmental degradation, on account of their high surface area to volume ratio and high reactivity. This tends to limit the potential practical applications and even scientific evaluation of the nanocrystalline properties [Host et al., 1998b; Hwang et al., 1997; Lu et al., 2005; Xiaomin et al., 2006]. The encapsulation of nanocrystal metal particles with chemically stable species, such as graphite carbon layers, has been a recent breakthrough in this regard [Hayashi et al., 1996; Hwang et al., 1997; Jiao & Seraphin, 1998 & 2000; Saito et al., 1994; Teng et al., 2007; Xiaomin et al., 2006]. Carbon encapsulated metal nanoparticles (CEMNs) may have applications in ferrofluids, sensor devices, hydrogen storage, xerography, micro-machinery, recording media, and biomedical applications [Ang et al., 2004; Flahaut et al., 2002; Host et al., 1997 & 1998a; Huo et al., 2007; Hwang et al., 1997; Seo et al., 2006; Setlur et al., 1998; Wang et al., 2003]. Among the many types of CEMNs with various core materials, those with iron group metals (nickel, cobalt, and iron) are of particular interest, not only because of their ferromagnetic properties, but also because these metals have a unique catalyzing ability to transform carbon into graphite [Ding et al., 2006; Dravid et al., 1995; Little, 2003; Lu et al., 2005; Saito et al., 1993a, 1993b & 1994; Seraphin et al., 1996; Setlur et al., 1998; Tomita et al., 2000; Wang et al., 2007].

The arc synthesis of CEMNs [Ang et al., 2004; Flahaut et al., 2002; Host et al., 1997, 1998a & 1998b; Hwang et al., 1997; Jiao and Seraphin, 1998 & 2000; Saito et al., 1993a & 1994; Teng et al., 2007; Tomita et al., 2000], which involves the evaporation of a metal-inserted graphite anode in an inert atmosphere, requires high power exceeding 1 kW and expensive vacuum systems to generate the plasmas [Host et al., 1997 & 1998b; Huo et al., 2007; Hwang et al., 1997; Jiao & Seraphin, 1998; Lu et al., 2005; Saito et al., 1994; Sano et al., 2002; Sergiienko et al., 2006; Wang et al., 2007]. Moreover, the arc method produces unwanted byproducts, such as carbon nanotubes and nanofibers, due to the harsh synthetic conditions arising from high energy generated during the process. Here we present the aerosol synthesis of CEMNs at ambient condition in a continuous manner through a nickel-graphite spark without the use of vacuum or special operating conditions. The morphology and structure of the synthesized particles were examined using high resolution transmission microscopy (HRTEM), selected area electron diffraction (SAED), energy dispersive X-ray spectroscopy (EDX), X-ray diffraction (XRD), and Raman spectroscopy. The particles were sampled on a porous carbon-coated copper grid located on a polyamide membrane filter (for use in HRTEM, SAED, and EDX) or on a glass plate (for use in XRD and Raman).

## 2.2 Materials and Methods

### 2.2.1 Preparations and characterizations of aerosol monometallic and bimetallic nanoparticles

The schematic setup for the spark generation is depicted in Figure 24. A spark was generated between two identical (homogeneous spark) or different (heterogeneous spark) metal rods (diameter: 3 mm, length: 100 mm, Nilaco, Japan) inside a generator (volume: 42.8 cm<sup>3</sup>) under a pure nitrogen environment (less than 10<sup>-4</sup> impurities) at STP [Byeon et al., 2006]. The flow rate of the nitrogen gas, which was controlled by a mass flow controller (MKS, US), was set to 3 L/min. The electrical circuit specifications were as follows: resistance of 0.5 M $\Omega$ , capacitance of 10 nF, loading current of 2 mA; applied voltage of 3.0 kV; and frequency of 667 Hz. The gas temperature inside the spark channel was increased beyond a critical value [Berkowitz & Walter, 1987], which was sufficient to sublime some parts of the electrodes. Since the duration of each spark was very short (~1.5 milliseconds) and the vapors were rapidly cooled after spark was generated, supersaturation was achieved and the nanoparticles were formed by nucleation/condensation. The generated particles carried by a flow of nitrogen and then sampled on a carbon-coated copper grid (for use in TEM and SEM analyses) and a glass fiber (for use in XRD analyses) located on a polytetrafluoroethylene (PTFE, for use in EDX and ICP-AES analyses) membrane filter in a sampler 20 cm downstream of the spark generator. The spark generator was periodically cleaned up with compressed dry particle-free air to eliminate the residual particles. Effluents from the sampler were passed through a high efficiency particulate air (HEPA) filter to remove potential non-sampled particles before releasing them into the laboratory hood via the exhaust system.

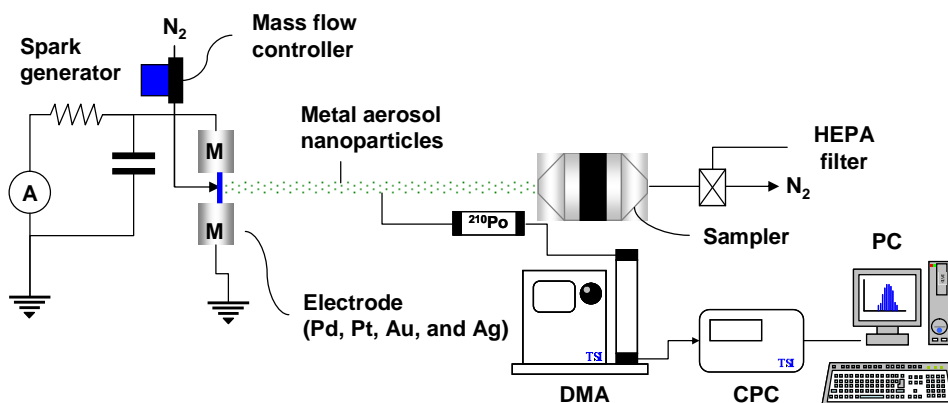


Figure 24. Schematic setup of spark generation.

The size distribution of the spark generated particles was measured by a SMPS system comprising an electrostatic classifier (3085, TSI, US), condensation particle counter (CPC, 3025, TSI, US), and aerosol charge neutralizer (Po-210). The SMPS system was operated with a sample flow of 0.3 L/min, sheath flow of 3 L/min, and scan time of 180 seconds (measurement range: 4.61-157 nm). The morphologies and corresponding selected area electron diffraction (SAED) patterns of the particles were analyzed using a HRTEM (JEM-3010, JEOL, Japan) operated at 300 kV. FESEM (JSM-6500F, JEOL, Japan) images and EDX (JED-2300, JEOL, Japan) profiles were obtained at an accelerating voltage of 15 kV. The generation rate and metal content of the particles were determined by ICP-AES (Elan 6000, Perkin-Elmer, US). A particles-sampled PTFE membrane filter was dissolved in concentrated acids medium ( $18 \text{ mol liter}^{-1} \text{ H}_2\text{SO}_4$ ,  $22 \text{ mol liter}^{-1} \text{ HF}$ ,  $14 \text{ mol liter}^{-1} \text{ HNO}_3$ ). Metal contents were obtained by comparison with standard solutions in the same medium. XRD studies of the

particles were carried out on a Rigaku RINT-2100 diffractometer equipped with a thin-film attachment using Cu- $K\alpha$  radiation (40 kV, 40 mA). The  $2\theta$  angles ranged from 10 to  $100^\circ$  at  $4^\circ/\text{min}$  by step scanning at an interval of  $0.08^\circ$ . The crystallite size of metal was calculated from the XRD spectra in accordance with Scherrer's formula.

## 2.2.2 Preparations and characterizations of aerosol carbon nanoparticles

A diagram of the experimental setup is shown in Figure 25. A cylindrical test duct with a volume of  $1,963 \text{ cm}^3$  (5 cm (D) $\times$ 100 cm (L)) with duralumin body was used for this study. The carbon particles were stably generated from the spark generator. Two cylindrical graphite rods (fine extruded, 6 mm (D)  $\times$  100 mm (L) each; Graphite Store, NC001310, US) were used as electrodes, which were positioned in a glass chamber of  $42.8 \text{ cm}^3$  volume. The spark generator was operated at atmospheric temperature and pressure and dry condition ( $< 1\%$  R.H.). The applied voltage of 2.5 kV caused spark discharge across the electrode gap, vaporizing material from the receiving electrode and producing carbon particles by nucleation of the vapor. These particles carried by a flow of nitrogen (purity of 99.9999%) entered the test duct.

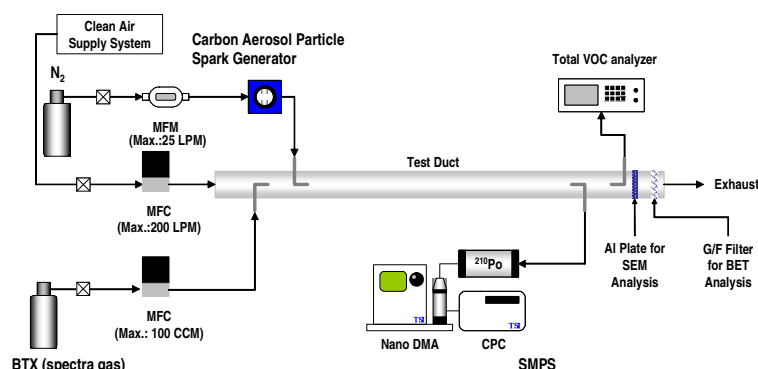


Figure 25. Experimental setup for tests of VOC adsorption-desorption.

The BTX gas with a mixing ratio of 0.47:0.45:0.09 was used as the reactant gas and was acquired from a compressed gas cylinder at concentration of 981.6 ppmv, with air as the balanced gas. Flow rates of the BTX gas stream and the particle free air stream were controlled by two mass flow controllers, respectively, while the nitrogen flow rate was controlled by a mass flow meter with a needle valve. The nitrogen flow rate ranged from 0.1 to 0.5 L/min, and the total flow rate ranged from 2 to 10 L/min.

The overall removal efficiency of VOC gas ( $\eta$ ) is defined as the difference in the BTX gas concentration between the inlet stream and the outlet stream.

$$\eta = (C_i - C_o) / C_i \quad (2)$$

where  $C_i$  and  $C_o$  are the inlet and the outlet BTX gas concentrations (ppmv), respectively. Concentrations of BTX gas were continuously measured by a photoionization detection (PID) gas analyzer (Kinsco Inc., Sniffer II, lower detection limit of 0.01 ppmv), which monitors TVOC at a sampling flow rate of 0.5 L/min.

The ratio between the supply rate of pore volume and the supply rate of BTX gas volume ( $R$ ) is

$$R = C_p Q V_p / C_i Q f_c \quad (3)$$

where  $C_p$  (mg/m<sup>3</sup>) is the mass concentration of the generated carbon particles,  $Q$  (m<sup>3</sup>/min) is the total-flow rate,  $V_p$  is the pore volume (m<sup>3</sup>/g) of the generated carbon particles, and  $f_c$  is the unit conversion factor ( $2.81 \times 10^{-4}$  m<sup>3</sup>-BTX mole/g-BTX mole). For complete removal of BTX gas ( $\eta=1$ ),  $R$  should be greater than 1, since all BTX gas molecules are supposed to be adsorbed on the pores of carbon particles.



BET surface area ( $\text{m}^2/\text{g}$ ), micropore area ( $\text{m}^2/\text{g}$ ), average pore diameter ( $\text{\AA}$ ), micropore volume ( $\text{cm}^3/\text{g}$ ), and total pore volume ( $\text{cm}^3/\text{g}$ ) of the particles were obtained by  $\text{N}_2$  adsorption at 77 K by using a micromeritics ASAP 2010. To determine the mass concentration of the particles ( $C_p$ ), size distribution and number concentration of the generated carbon particles were measured by a SMPS system at a sampling flow rate of 0.3 L/min. SEM of the generated particles were obtained by using a SEM apparatus (Cambridge S250 MK2, operated at 20kV).

### 2.2.3 Preparations and characterizations of aerosol CEMNs

In our spark generation apparatus, the spark was generated between a metal (Ni, Co, or Fe) and graphite rod (each; 3 mm diameter, 100 mm length, Nilaco, Japan) in a chamber under a pure nitrogen (less than  $10^{-4}$  impurities) atmosphere at STP [Byeon et al., 2006]. The spark was generated by a current of 2 mA; a voltage drop of 2.4 kV with a frequency of 667 Hz between the electrodes was kept stable by continuously translating the graphite rod to the metal rod to keep a constant distance (1 mm). The spark channel increased the gas temperature within the channel to above a critical value [Berkowitz & Walter, 1987] sufficient to sublime parts of the electrodes. Since the duration of each spark was quite short ( $\sim 1.5$  milliseconds) and the vapors cooled rapidly after the spark, a supersaturation was achieved and the particles were formed by nucleation/condensation [Horvath & Gangl, 2003]. These thermal processes [Artamonov et al., 2001; Krasik et al., 2006] usually occur near the anode, which is heated as a result of the fast collisions of energetic electrons, resulting in a relatively strong spark channel near the anode. Particles are also generated near the cathode through thermal processes similar to those occurring near the anode in addition to sputtering by ionic bombardment [Borra et al., 1998]. The nitrogen gas flow carried the spark generated particles as they exited the spark

chamber. The nitrogen gas flow rate was 0.5 L/min. The chamber was cleaned periodically with compressed dry particle-free air to eliminate the residual particles.

The non-purified spark generated particles were analyzed using various methods. High resolution transmission electron microscopy (HRTEM, JEM-3010, JEOL, Japan) was operated at 300 kV with electron diffraction and energy dispersive X-ray spectroscopy (EDX, Oxford). The selected area electron diffraction (SAED) patterns of the particles were used to determine the crystalline phase. The interlayer spacing of the particles was calculated using digital micrograph software and TEM. The EDX patterns of the selected local areas were used to determine the elemental composition of the particles. X-ray diffraction (XRD, Rigaku D/max-2100, Japan) operated with CuK $\alpha$  radiation ( $\lambda=154.178$  pm) at a step size of  $0.08^\circ$  was used to analyze the phases. Raman spectroscopy (T64000, HORIBA Jobin Yvon, France) was used to determine the level of graphitization in the particles. The laser excitation wavelength was 514.5 nm.

## 2.3 Results and discussion

### 2.3.1 Properties and mechanisms of SGs aerosol monometallic and bimetallic nanoparticles

Figure 26 shows the particle size distributions of spark generated monometallic aerosol nanoparticles. The geometric mean diameters and total number concentrations for Pd, Pt, Au, and Ag homogeneous sparks were 26.7 and  $3.36 \times 10^6$ , 37.7 and  $5.60 \times 10^6$ , 48.8 and  $7.75 \times 10^6$ , and 14.9 nm and  $9.45 \times 10^5$  particles/cm<sup>3</sup>, respectively, and the order of particle concentrations was Au > Pt > Pd > Ag although operation conditions of each spark were same.

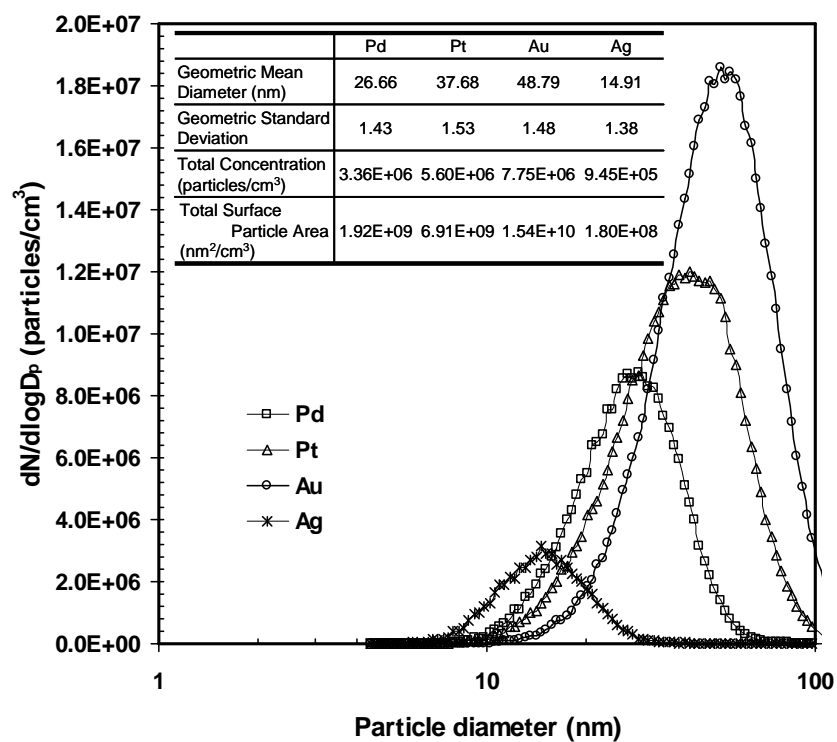


Figure 26. Particle size distributions of monometallic nanoparticles.

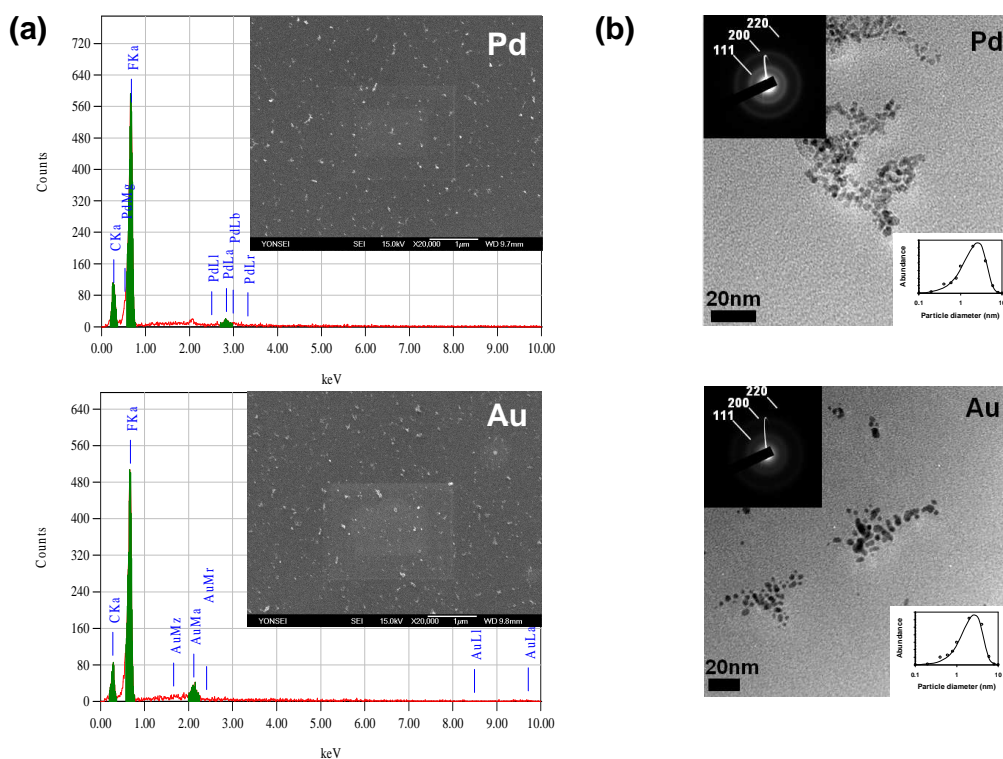


Figure 27. Morphological, chemical and structural results of Pd and Au monometallic nanoparticles. (a) SEM micrographs and EDX profiles. (b) TEM micrographs and SAED patterns.

Figure 27 shows the morphological, chemical, and structural results of the monometallic nanoparticles. Here, the results only for the Pd and Au particles by reason of no remarkable morphological differences were shown among the Pd, Pt, Au, and Ag particles. Both SEM micrographs (inset of Figure 27(a)) for the Pd and Au show that the particles existed as a form of agglomerate consisted of several primary particles. The mean sizes of the Pd and Au agglomerated particles are ~25 and ~45 nm, respectively, and the sizes are well

corresponded to the results in Figure 26. Figure 27 also shows EDX profiles of the Pd and Au particles. From the EDX profiles, it was found that each case contained Pd and Au, respectively. Figure 27(b) shows the TEM micrographs, which clearly reveal the spherical-shaped primary particles for the Pd and Au in agglomerate. Size distributions of each primary particle also depicted in the TEM micrographs, the mean diameters of Pd and Au particles are 2.6 and 3.5nm, respectively. Both SAED patterns (also shown in Figure 27(b)) of the Pd and Au particles have clear diffraction Debye-Scherrer rings showing [111] and [200] reflections and weak diffraction ring shown [200] of the fcc lattices of metallic Pd and Au. This indicates that spark generated particles are pure crystallites.

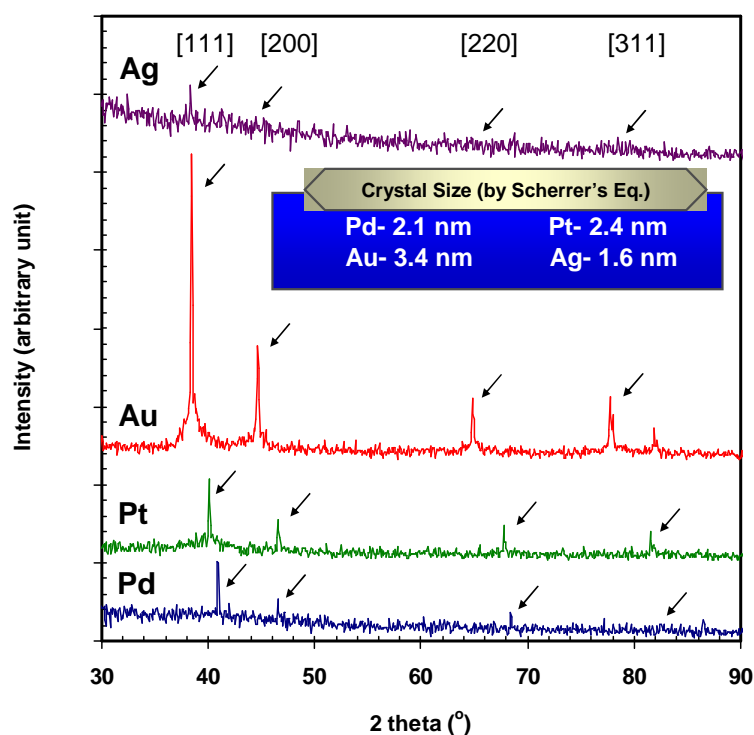


Figure 28. X-ray diffractograms of monometallic nanoparticles.

To clearly distinguish the crystalline phase of the monometallic particles, further measurements the X-ray diffractions (Figure 28) of the Pd, Pt, Au and Ag particles were performed. Four characteristic peaks for Pd ( $2\theta = 40.1, 46.7, 68.1$ , and  $82.1^\circ$ ), Pt ( $2\theta = 39.8, 46.2, 67.4$ , and  $81.3^\circ$ ), Au ( $2\theta = 38.2, 44.4, 64.6$ , and  $77.5^\circ$ ), and Ag ( $2\theta = 38.1, 44.3, 64.4$ , and  $77.5^\circ$ ) marked by their indices of [111], [200], [220], and [311] were observed. These also revealed that the spark generated particles are pure fcc metals. The sharpness (Au > Pt > Pd > Ag) of the peak is the highest for Au because of the largest amount of the Au particles. Furthermore, the average crystallite sizes were evaluated according to Scherrer's formula and the results are also shown in Figure 28. The average sizes were slightly smaller than those in TEM results. This might be due to an interference of glass fiber (containing silica and impurities) during the measurement.

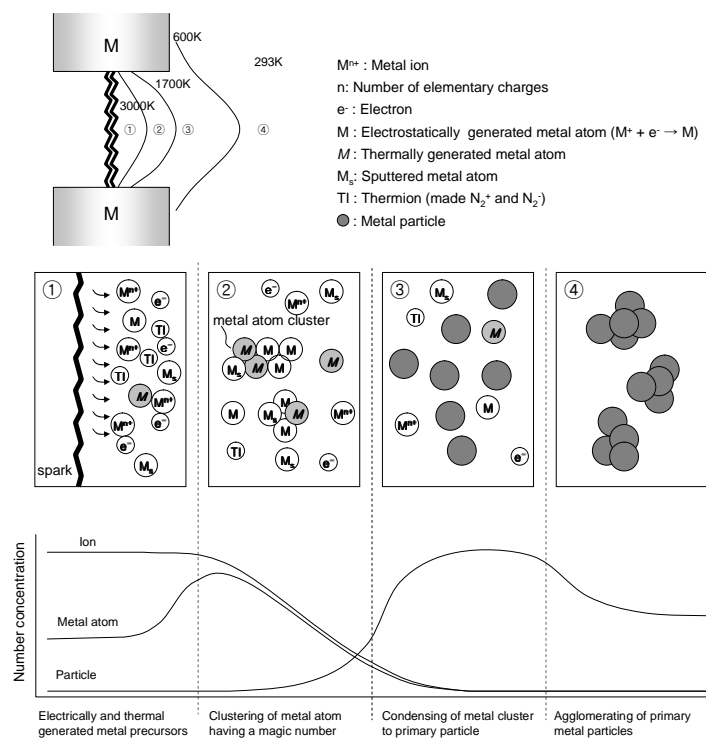


Figure 29. Mechanism of spark generated monometallic nanoparticles.

A proposed mechanism of the monometallic particles during the spark generation is depicted in Figure 29. The mechanism can be best understood by proceeding along the two routes for metal atom (to be condensed to solid particle) generation during the process. One is the electrostatic atom generation via reduction of metal ion and sputtering of material; the other is the thermal atom generation. The certain applied voltage caused spark generation across the electrode gap, and the energetic electron collision (near the anode) [Artamonov et al., 2001; Holland, 1956; Krasik et al., 2006; Marusina & Filimonenko, 1984] and ion bombardment (sputtering, near the cathode) [Borra et al., 1998] are performed, and thus high temperature spark channel can be formed. The temperature profile (as shown in Figure 29) of the spark generator was calculated for an assumed temperature (5,000 K) of the spark channel using a commercial computational fluid dynamics (CFD) code (Fluent 6.3) with a finite volume grid containing approximately 9,000 cells. Near the spark channel, vapor containing highly ionized (metal ion) and neutral (metal atom) metal species [Krasik et al., 2006] exists in direct spatial coincidence with the channel. While the vapor is transported by nitrogen gas to exit of the spark generator, where cluster growth (nucleation) having magic number of metal atom to be formed the primary particle [Harada et al., 2005; Oleshko, 2006] occurs under a condition of high supersaturation, and follows homogeneous condensation. When the vapor temperature reaches at the certain low point by nitrogen flow, the cluster condensed to primary metal particle while residual ionized species and atoms may also flow out of the spark generator. The concentration of primary particles could be determined by amount of condensed clusters during the condensation process [Wang et al., 2001]. As discussed earlier (Figure 26), the amount of the particles is in order of Au > Pt > Pd > Ag. This corresponds that the highest amount of clusters existed for the Au spark. According to known mechanism [Artamonov et al., 2001; Krasik et al., 2006] of spark generation, this ordering may be due to

several parameters, such as melting (thermodynamic) point, ionization potential [Neogrdy et al., 1997], and sputtering rate [Mizsei et al., 1998] of materials. Table 6 displays the above parameters relating to the results for the particle generation. From either thermodynamic or sputtering point of view, Ag particle enrichment could be foreseeable but this expectation mismatched to results of the particle generations. This indicates that particle generation characteristics (or rates) depended on neither melting point nor sputtering rate of electrode material. On the other hand, ionization potentials of the electrode materials are well matched to the generations. The ionization potential of an atom is the energy required to remove of electrons from isolated gaseous atoms, and substantially, the higher ionization potential of the material favors to the particle enrichment in the spark generation [Harada et al., 2005; Wang et al., 2006]. The ionization potential of Ag atom (7.58 eV) is known to be the lowest in the experiments (Au: 9.22 eV, Pt: 9.00 eV, Pd: 8.23 eV). This means that Ag spark has the highest concentration of highly ionized silver ions due to its low ionization potential, so atom formation (reduction of Ag ion) rate was the slowest in the experiments, subsequently, the lowest concentration of clusters (multi-atom structure with a magic number to be condensed) were formed at the early period of the condensation. For the Au case, having the highest ionization potential in the experiments, the atom formation rate of Au ion is the fastest, and subsequently, the highest amount of Au atoms is formed before the formation of cluster. Finally, different cluster concentrations of the electrode materials possibly followed the different particle generation rates ( $Au > Pt > Pd > Ag$ ). To verify this description, ion concentration in effluents of the spark generations was also checked, and the data also displayed in Table 6. Unfortunately, we could not found a correlation between particle generation and residual ion concentration under ionization potential point of view, by this approach, the highest particle generation rate could be followed the lowest residual ion



concentration. One possible reason for this mismatch is an unconsidered coincidence of residual metal ions and thermally generated ions [Jiang et al., 2007; Maricq, 2005] (i.e. nitrogen ions) during the spark generation, this coincidence might be redistributed the residual ion concentration. Correspondingly, the spark generated particles were electrically charged with the Boltzmann charge distribution (or electrically neutral state); this result is a general phenomenon for particle generation under high temperature environment.

Table 6 Generation rates of monometallic nanoparticles with relating parameters

Element	Melting point (K)	Relative sputtering rate	Ionization potential (eV)	Particle generation rate (mg/min)	Residual ion concentration (ions/m <sup>3</sup> )
Pd	1828.0	0.85	8.33	$1.68 \times 10^{-3}$	$1.2 \times 10^{11}$
Pt	2041.4	0.60	9.00	$1.60 \times 10^{-2}$	$2.2 \times 10^{11}$
Au	1337.3	1.00	9.22	$4.03 \times 10^{-2}$	$1.6 \times 10^{11}$
Ag	1234.9	1.20	7.58	$1.22 \times 10^{-4}$	$1.0 \times 10^{11}$

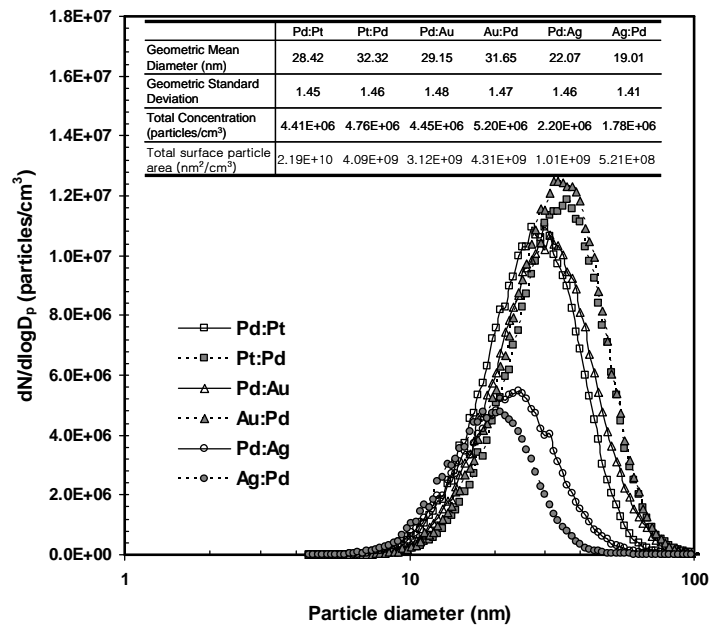


Figure 30. Particle size distributions of bimetallic nanoparticles.

Figure 30 shows the particle size distributions of spark generated bimetallic aerosol nanoparticles. The geometric mean diameters and total number concentrations for Pd:Pt, Pt:Pt, Pd:Ag, Au:Pt, Pd:Ag, and Ag:Pt (denoted the anode:cathode of spark set) heterogeneous sparks were 28.4, 32.3, 29.2, 31.7, 22.1, and 19.0 nm, and 4.41, 4.76, 4.45, 5.20, 2.20, and  $1.78 \times 10^6$  particles/cm<sup>3</sup>, respectively. The size distributions are located at between each monometallic particle size distribution as shown in Figure 26. These locations originated from a simple mixing of high and low amounts generating spark electrode materials. Furthermore, the diameters and concentrations of the particles changed by switching the electrode polarity because of a work difference between anode [Artamonov et al., 2001; Holland, 1956; Krasik et al., 2006; Marusina & Filimonenko, 1984] and cathode [Borra et al., 1998]. A thermal process preferentially occur near the anode where was heated due to fast collisions of energetic electrons, resulting in relatively strong spark channel near the anode. Corresponding mass fractions and generation rates are displayed in Table 7. For Pd-Pt and Pd-Au sparks, mass fractions of anode materials are higher than those of cathode materials. On the other hand, for Pd-Ag sparks (Pd:Ag and Ag:Pt), Pd has higher fraction than Ag (although Ag fraction was slightly changed from 0.15 to 0.25) regardless of electrode polarity. This may be due to a great difference of particle generation rate between Pd and Ag.

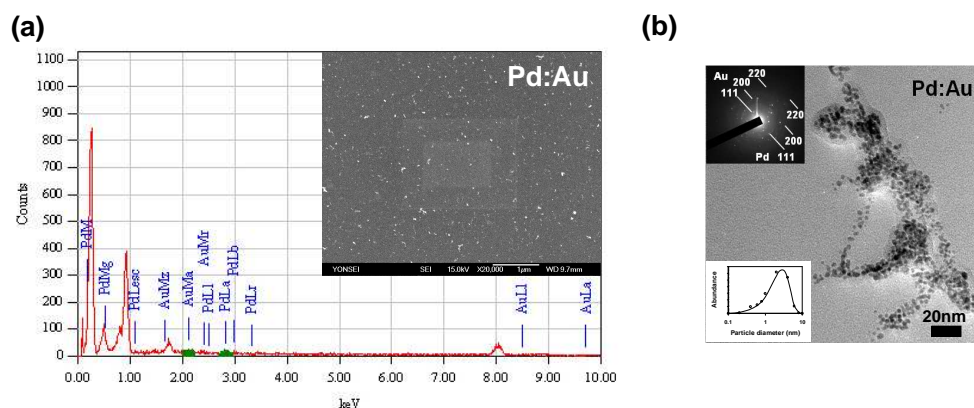


Figure 31. Morphological, chemical and structural results of Pd:Au bimetallic nanoparticles.

(a) SEM micrograph and EDX profile. (b) TEM micrograph and SAED pattern.

Table 7 Metal fractions and generation rates of bimetallic nanoparticles

Element (M1:M2)	Mass fraction (M1:M2)	Particle generation rate (mg/min)
Pd:Pt	0.52:0.47	$2.64 \times 10^{-3}$
Pt:Pt	0.68:0.32	$6.28 \times 10^{-3}$
Pd:Au	0.59:0.41	$3.78 \times 10^{-3}$
Au:Pt	0.70:0.30	$6.88 \times 10^{-3}$
Pd:Ag	0.85:0.15	$6.62 \times 10^{-4}$
Ag:Pt	0.25:0.75	$2.81 \times 10^{-4}$

Figure 31 shows the morphological, chemical, and structural results of the bimetallic Pd:Au nanoparticles, which followed the results of monometallic Pd and Au monometallic nanoparticles. The SEM micrograph (Figure 31(a)) shows the agglomerate particles, and its result is not considerably different from monometallic particles as shown in Figure 27(a). The mean size of the Pd:Au agglomerate particles is approximately 34 nm, and the size is well

corresponded to the results in Figure 30. Corresponding EDX profile suggested that both Pd and Au particles are contained in the agglomerate particles. The TEM micrograph (Figure 31(b)) demonstrates that the bimetallic particles are composed of ultrafine spherical particles of almost uniform size (2-4 nm) although an accurate identification whether binary mixture or alloy is difficult. Figure 31(b) also shows the corresponding SAED pattern to the TEM micrograph, this pattern consists of overlapping ring dots of the individual monometallic particles of Pd and Au, showing [111], [200], and [220] reflections of the fcc lattice of monometallic Pd and Au. This indicates that the resultant Pd:Au particles are not alloyed, and have a structure similar to the physical mixing or gathering of monometallic Pd and Au particles prepared separately.

In order to clearly examine whether the bimetallic particles are a binary mixture or are an alloy, further measurements the X-ray diffractions (Figure 32) of the Pd:Pt, Pd:Au, and Pd:Ag particles were performed. The diffraction patterns of all the bimetallic particles consisted of two consecutive peaks at [111], [200], and [220] planes for two individual materials while the diffractograms obtained for bimetallic particles do not show any other additional peak, indicating the formation of simple bimetallic mixture, not alloy phase. A lack of thermal energy during the particle formation leads to a mixing of monometallic particles. Therefore, it could be concluded that particles are stably existed as monometallic phase during the heterogeneous spark generations and then agglomerated each other. Peak broadening analyses on [111] peaks of all the bimetallic particles indicated an average crystal size ranging from 2 to 4 nm (from Ag:Pt to Au:Pt), indicating that the crystal sizes are comparable with those TEM results. Furthermore, for Pd(-) heterogeneous sparks, having different metal fractions from Pd(+) heterogeneous sparks, as shown in Figure 32, locations of their peaks

were same with the Pd(+) sparks but their intensities changed due to the different metal fractions (not shown in Figure 32).

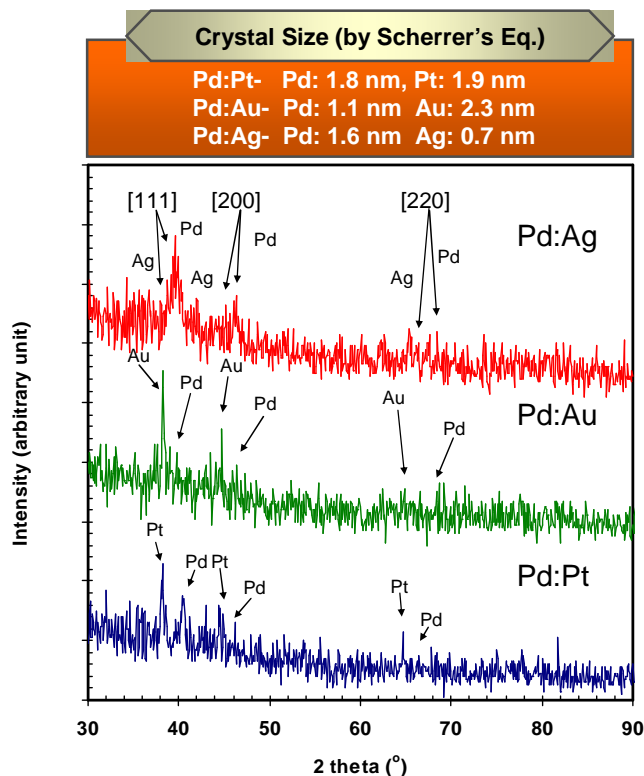


Figure 32. X-ray diffractograms of bimetallic nanoparticles.

Based on the results, a mechanism of the bimetallic nanoparticles during the heterogeneous spark generation (Figure 33) was proposed. General mechanism is similar to the previous description (Figure 29), so in this description focused on the formation of mixture (not alloy) bimetallic nanoparticles. Before condensation, two metal atoms were co-existed as gas phase in spark channel, and, subsequently, M1s (having higher melting point) are separated (or expelled) from M1s+M2s atom cloud due to a thermophoretic effect at early period of condensation, indicating the no diffusion of M1 into M2 matrix. The expulsion is a common

phenomenon in alloy systems, and might be driven by a number of factors, such as surface energy, affinity of gases, heat of melt (or sublimation) and strain energy [Wang et al., 2006]. In the experiments, different melting point between co-existed two materials might drive the expulsion by existing  $N_2$  gas flow. When is subjected to condensing (or quenching) the metal atoms, since the melting point of M1 is higher than M2, M1s will migrate from M1s+M2s atom cloud to outer region due to thermophoretic effect. The separated atoms (M1 and M2) with each magic number then subsequently condensed to each monometallic primary particle at low temperature region. Two monometallic particles are then agglomerate together to form larger particles.

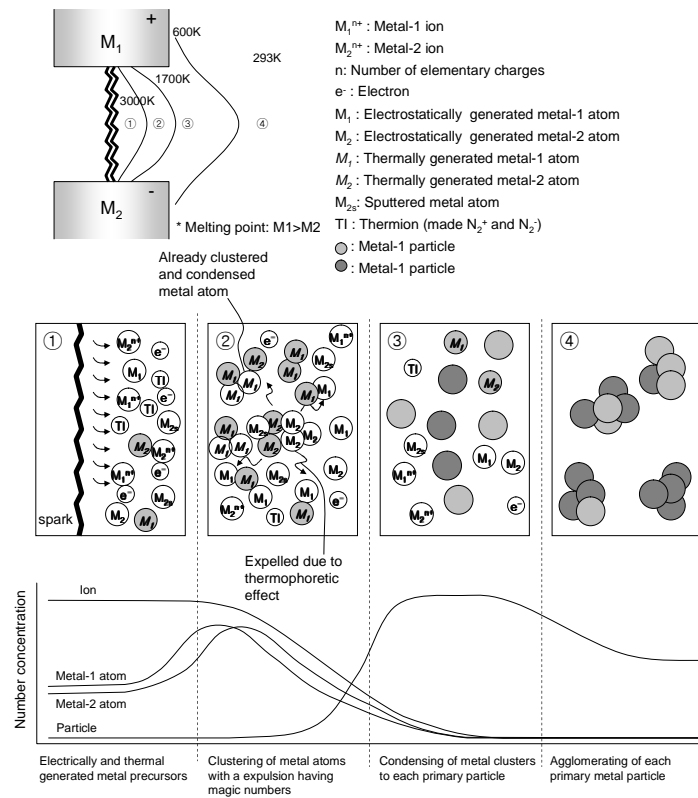


Figure 33. Mechanism of spark generated bimetallic nanoparticles.

### 2.3.2 Textural properties and VOC removal of SG aerosol carbon nanoparticles

The size distribution of the particles obtained by SMPS is shown in Figure 34. The size ranged from several tens to hundreds of nanometers and their geometric mean diameter was about 95 nm, resulting in the total mass concentration of about 1.31 g/m<sup>3</sup>. Figure 34 also shows a SEM micrograph ( $\times 20,000$ ) of carbon particles. It was expected that the aggregates, composed of primary nanoparticles, might contribute to the increase of the BET surface area and total pore volume, and thus, to higher chance of VOC adsorption onto the carbon particles.

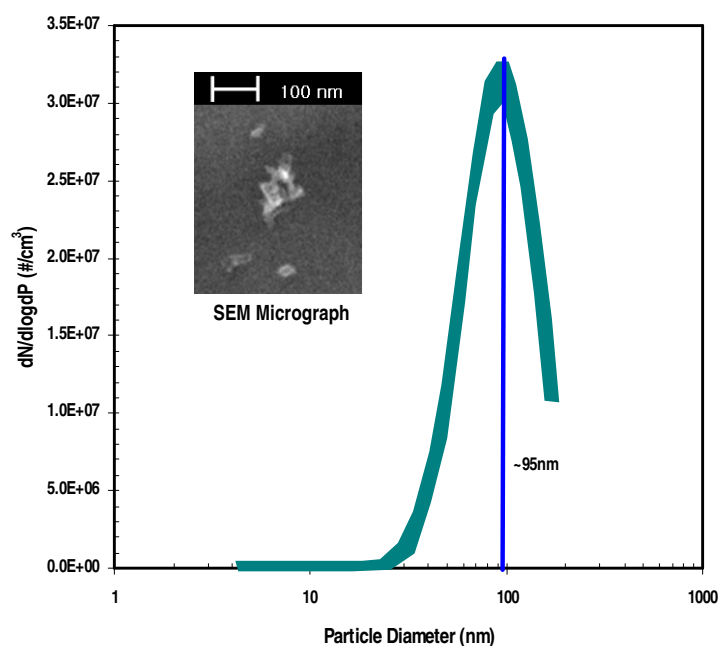


Figure 34. Morphology and size distribution of generated carbon particles.

Table 8 summarizes the characteristics of the carbon graphite electrode, spark generated carbon particles, and conventional activated carbon. Table 9 summarizes the data of  $\eta$  and R for BTX gas. The total pore volume (for  $<769 \text{ \AA}$  of pore size) of 1.62 cm<sup>3</sup>/g and

micropore volume ( $<20.9 \text{ \AA}$ ) of  $0.033 \text{ cm}^3/\text{g}$  were used in the calculations of  $R_T$  and  $R_M$  (refer to Eq.(3)), respectively. The theoretical value of  $R$  required for the complete removal of BTX gas is 1.0 if all gas molecules are assumed to be adsorbed in all the pores of carbon particles. For  $R_T$ , however, the removal efficiency  $\eta$  for 0.983 minutes of residence time and 0.5 ppmv of BTX gas initial concentration was 4%, even though the supply rate of pore volume was 4.24 times higher than the supply rate of BTX gas volume. Such a low removal efficiency might be caused by inadequate BTX gas-to-particle collisions, which depend on the pore size distribution of the particles. When the residence time was 0.483 or 0.2 minutes for 0.5 ppmv of BTX gas concentration, the removal efficiency could not be obtained due to the relatively shorter particle residence time. With 1.0 ppmv BTX gas, the removal efficiency could not be obtained, regardless of residence time, due to detectable limit of the gas analyzer.

Table 8 Properties of the graphite rod, the generated carbon particles, and conventional activated carbon

Samples	BET Surface Area ( $\text{m}^2/\text{g}$ )	Micropore Area ( $\text{m}^2/\text{g}$ , $< 20.9 \text{ \AA}$ )	Microporosity (%)	Average Pore Diameter ( $\text{\AA}$ )	Micropore Volume ( $\text{cm}^3/\text{g}$ )	Total Pore Volume ( $\text{cm}^3/\text{g}$ , $< 769 \text{ \AA}$ )
Carbon Graphite Electrodes	6.66	0.24	3.54	118	~0	0.012
Spark Generated Carbon Particles	639	29	4.51	104	0.033	1.62
Conventional Activated Carbon	800-1,500	300-1,000	20-60	~20	0.3-1.4	0.5-2.0

The values of  $R_M$  were obtained with Eq.(3) based on micropore volume, rather than the total pore volume, and are also listed in Table 9. All the values of  $R_M$  are much lower than 1.0. Therefore, such a low removal efficiency of 4% might be caused by the insufficient supply



of micropore volume of carbon particles, even though the total pore volume and the BET surface area of the particles were similar to those of conventional activated carbon. One possible reason for this problem is the ineffective pore size distribution of the carbon particles for BTX gas adsorption as a result of ineffective interstitial behavior among the primary carbon particles.

Table 9 Data  $\eta$  and R based on pore volume

Residence Time (min) [Total-Flow Rate (L/min)]	0.5ppmv			1.0ppmv		
	$\eta$	$R_T$	$R_M$	$\eta$	$R_T$	$R_M$
0.983 [ 2 ]	0.04	4.24	0.086	ND	2.12	0.043
0.483 [ 4 ]	ND	4.09	0.083	ND	2.07	0.042
0.200 [ 10 ]	ND	4.03	0.082	ND	2.01	0.040

\* ND: Not Detected

The pore size distribution of the carbon particles that were collected on a glass fiber filter is shown in Figure 35. As discussed with Table 9, the micropore volume of the carbon particles was very small compared to that of a conventional activated carbon. Much higher micropore volume of the particles would result in higher removal efficiency.

Conclusively, the use of the spark generator slightly enhanced the removal of the BTX gas (4% of removal efficiency) because the spark generator produced insufficient micropore volume of the generated carbon particles compared to that of conventional activated carbon. To increase the micropore volume would require the change of characteristics of carbon

aerosol particles, including size distribution and morphology, by modifying the spark generation system.

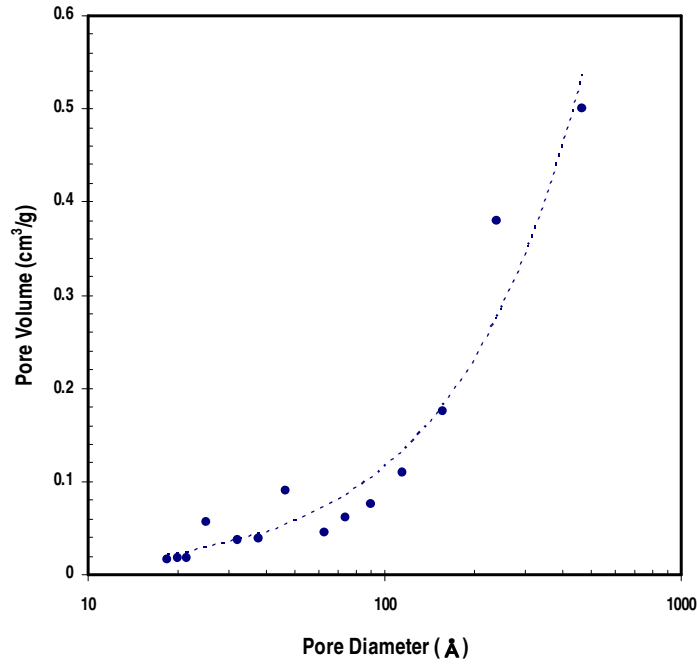


Figure 35. Pore size distribution of generated carbon particles.

### 2.3.3 Properties and mechanisms of SGs aerosol CEMNs

Figure 36(a) shows a TEM image of the spark generated particles from nickel (anode) and graphite (cathode) electrodes. The inset in Figure 36(a) shows the local EDX information, indicating the presence of nickel and carbon. The other peak around 8.00 keV corresponds to the copper grid used to support the sample. Two hundred particles in Figure 36(a) were selected and their sizes were measured from the TEM images. The sizes ranged from 10 to 390 nm in diameter (geometric mean diameter = 86 nm), and are shown in the inset of Figure 36(b). Figure 36(b) shows a TEM image of one of the particles. Figure 36(b) clearly shows the

particle to consist of a core and shells. The SAED pattern for the particle shown in Figure 36(c) demonstrates that the particle consists of pure nickel and carbon. Since the TEM image reveals the core to be darker than that of the shell, it is clear that the particle has a nickel core with a graphitic shell. The diffraction pattern is a superposition of the two sets of patterns: one is a set of annular rings originating from turbostratic carbon (diffraction from a two-dimensional lattice), and the other spots from a single nickel crystal (arranged in rectangular lattice). The diffraction rings corresponding to a layer distance of approximately 0.34, 0.18, and 0.17 nm are considered to be the [002], [102], and [004] planes of hexagonal graphite, respectively. On the other hand, the layer distances of approximately 0.11, 0.08, and 0.06 nm were assigned to the [311], [420], and [440] planes of face-centered cubic (fcc) nickel crystalline, respectively. The parallel fringes in the shell (Figure 36(d)) show that they are ordered graphitic nanostructures. These contiguous carbon fringes around a nickel core are evidence for the complete encapsulation by a graphitic shell. Previous studies [Host et al., 1998a & 1998b; Little, 2003; Saito et al., 1993b; Xiaomin et al., 2006] reported that these graphite-metal nanostructures are formed as a result of the catalytic effect of a metal on carbon. In this system (Figure 36(e)), when a spark channel was formed between the nickel and graphite electrodes, parts of the electrodes were evaporated due to the high temperature of the spark. The condensation temperature of carbon is higher than that of nickel. Therefore, the condensation of carbon vapor to liquid progresses more rapidly than nickel when the vapors are swept out from the spark channel by the nitrogen gas flow. In this progress, liquid carbon was pushed from the vapor nickel toward the interface where the vapor nickel was surrounded by nitrogen gas due to the temperature gradient from the vapor nickel to the nitrogen gas. Simultaneously, the vapor nickel near the interface began to condense into a liquid during the carbon movement [Baker, 1989; Holstein, 1995] and the liquid carbon was prevented from

moving away from the interface due to its high affinity to nickel. The catalytic ability of nickel then caused carbon graphitization. Further cooling by nitrogen gas flow induced the solidification of liquid nickel. Eventually, the graphitization ceased when the leading solid nickel surface was encapsulated by formerly formed graphitic shells, which prevented further graphitization. During graphitization, the remaining liquid nickel was completely solidified and its volume decreased. Hence, an empty zone was formed between the graphitic shells and the solid nickel core. Figure 36(f) shows the number of graphitic shells and the nickel-to-carbon mass fraction as function of the CEMN diameter or nickel core diameter. Both the number of graphitic shells and the nickel-to-carbon mass fraction increased with increasing the nickel core diameter, as observed in other materials [Host et al., 1997; Hwang et al., 1997; Jiao & Seraphin, 2000; Wang et al., 2003]. When the amount of nickel vapor was insufficient, the unreacted liquid carbon escaped from the interface and become solid carbon in the nitrogen gas flow. Figure 36(g) shows that the debris particles in Figure 36(a) were aggregates. The inset in Figure 36(g) revealed the debris to be disordered graphitic nanostructures. The XRD profile (Figure 36(h)) indicates that the cores of the particles shown in Figure 36(a) are element nickel. There is a relatively broad peak at  $2\theta = 26.1^\circ$ , which is close to  $2\theta = 26.4^\circ$  for graphite with a  $d$  value of 0.341 nm and slightly larger than the 0.336 nm ( $d_{002}$ ) for graphite. The broad diffraction peak indicates that the graphite also has a disordered structure. The large intershell distance suggests a reduction in the intershell interaction compared with perfect graphite. The two subsidiary peaks at  $2\theta = 44.3^\circ$  and  $54.3^\circ$  correspond to the [110] and [004] crystal planes of graphite, respectively. Another peak at  $2\theta = 44.5^\circ$  (with  $d$  value is 0.2022 nm, which is almost consistent with the  $d_{111}$  (0.2034 nm) of nickel),  $51.8^\circ$ , and  $76.4^\circ$  were respectively attributed to the [111], [200], and [220] crystal planes of fcc-nickel metal, respectively. The Raman spectrum (Figure 36(i)) shows that the G band (stretching vibrations

in the basal plane of crystalline graphite) is close to  $1582\text{ cm}^{-1}$ , with a similar shape to that reported elsewhere [Flahaut et al., 2002; Lu et al., 2005; Seo et al., 2006; Xiaomin et al., 2006], suggesting that the structure of the sample was well oriented, and had a chemical structure similar to that of a graphite layer. In addition, the D band ( $1343\text{ cm}^{-1}$ , indicating the level of defects in the graphitic material) might have originated from the disordered or defective parts of the CEMNs (corners and edges) [Host et al., 1997; Hwang et al., 1997; Saito et al., 1993a & 1993b; Sano et al., 2002] and debris around the CEMNs.

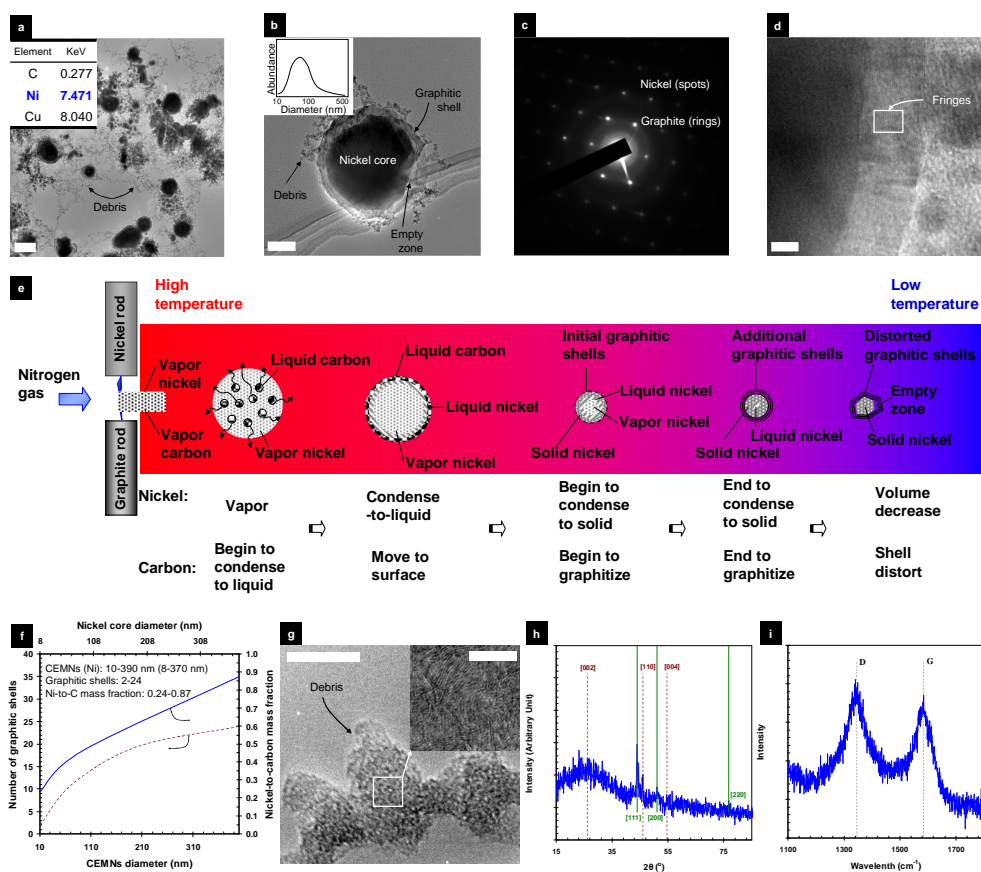


Figure 36. Spark generated particles (anode: Ni, cathode: C) and their characterization. (a) TEM image with local EDX information of the spark generated particles. Scale bar, 200nm. (b) TEM image of a single core-shell shaped particle with the size distribution. Scale bar, 20 nm. (c) SAED pattern of the particle in Figure 1(b). (d) High magnitude TEM image of the particle. Scale bar, 5 nm. (e) Formation mechanism of the CEMNs. (f) Number of graphitic shells and the nickel-to-carbon mass fraction for CEMNs. (g) High magnitude TEM images of the debris. Scale bars, 10 nm and 5 nm (inset). (h) XRD pattern of the spark generated particles. (i) Raman spectrum of the spark generated particles.

The experiments were also carried out for the configuration of the nickel (cathode)-graphite (anode) electrodes. In this configuration, the nickel-to-carbon mass fraction was 6.4%, while the mass fraction for the configuration of nickel (anode)-graphite (cathode) electrodes was 18.7%. Likewise, the yield of CEMN from the nickel (anode)-graphite (cathode) electrodes was higher (54%) than that of nickel (cathode)-graphite (anode) electrodes (18%). The yield was determined from the area fraction of CEMNs-to-all particles in the TEM image. If insufficient nickel is present, the unreacted carbon would form debris and co-exist with the CEMNs in the aerosol state as they are forced away from the spark channel by the gas flow.

More experiments with other metal particles, such as cobalt and iron, were carried out. Although these cobalt and iron cases were prepared under the same processing conditions as that for nickel, the properties of the particles were slightly different from those in the nickel case. Information on the details is available on Science Online. This method for preparing CEMNs was simple, continuous, and practical compared with conventional methodologies, and can be applied to the production of nanocrystal encapsulates.

## 2.4 Summaries and conclusions

The generation and characterization of monometallic (palladium, platinum, gold and silver from homogeneous spark sets) and bimetallic (palladium-platinum, palladium-gold and palladium-silver from heterogeneous spark sets) nanoparticles dispersed in nitrogen gas by spark generation method were reported. Morphology and structure of the particles were spherical-shaped and fcc crystallite, respectively, and the primary sizes of most particles ranged from 2 to 4 nm (silver < palladium < platinum < gold) in diameter and their sizes increased up to several tens of nanometer due to an agglomeration occurrence among the primary particles. For monometallic particles, the particle size-generation rate of palladium, platinum, gold, and silver homogeneous sparks were  $26.7\text{--}1.68 \times 10^{-3}$ ,  $37.7\text{--}1.60 \times 10^{-2}$ ,  $48.8\text{--}4.03 \times 10^{-2}$  and  $14.9\text{ nm--}1.22 \times 10^{-4}$  mg/min, respectively. The ionization potentials (gold: 9.22 > platinum: 9.00 > palladium: 8.33 > silver: 7.58 eV) of the metals were well matched with the generation rates. For bimetallic particles by heterogeneous sparks, the resultant bimetallic particles were characterized to be mixtures (not alloys) of different metal particles with a face-centered cubic structure. By changing the spark sets from Pd(+):Pt(-), Pd(+):Au(-) and Pd(+):Ag(-) to Pd(-):Pt(+), Pd(-):Au(+) and Pd(-):Ag(+), the particle generation rate-metal fraction varied from  $2.64 \times 10^{-3}\text{--}0.52\text{:}0.48$ ,  $3.78 \times 10^{-3}\text{--}0.59\text{:}0.41$  and  $6.62 \times 10^{-4}$  mg/min-0.85:0.15 to  $6.28 \times 10^{-3}\text{--}0.32\text{:}0.68$ ,  $6.88 \times 10^{-3}\text{--}0.30\text{:}0.70$  and  $2.81 \times 10^{-4}$  mg/min-0.75:0.25, respectively.

All the values of the ratio between the supply rate of micropore volume and the supply rate of BTX gas volume are much lower than 1.0. Therefore, such a low removal efficiency of 4% might be caused by the insufficient supply of micropore volume of carbon particles, even though the total pore volume and the BET surface area of the particles were similar to those of conventional activated carbon. One possible reason for this problem is the ineffective pore size

distribution of the carbon particles for BTX gas adsorption as a result of ineffective interstitial behavior among the primary carbon particles.

The geometric mean diameter of CEMNs from the nickel (anode)-graphite (cathode) spark electrodes was 86 nm. The electron and X-ray diffraction patterns showed that both nickel and graphite in the sample were pure elements. The Raman peaks at  $1582\text{ cm}^{-1}$  (G-band) and  $1343\text{ cm}^{-1}$  (D-band) demonstrated the particles to have an  $I_G:I_D$  ratio of 0.81, where  $I_G$  and  $I_D$  are the intensities of the G and D peaks, respectively. The nickel-to-carbon mass fraction for the spark electrodes was 18.7%, while the mass fraction for the configuration of nickel (cathode)-graphite (anode) spark electrodes was 6.4%. Likewise, the yield of CEMN from the nickel (anode)-graphite (cathode) electrodes was higher (54%) than that of nickel (cathode)-graphite (anode) electrodes (18%).



### **3. Nanoparticle synthesis by combining of SG and ELD**

#### **3.1 Introduction**

##### **3.1.1 Catalytic surface activation via aerosol palladium (Pd) nanoparticles for use in Ag ELD onto ACF**

The ELD of metal is a simple chemical process for depositing metal layers onto nonconductive or conductive materials with complicated configurations that are widely used in automotives, aerospace, packaging, appliances, optics, and electronics industries [Metz et al., 2007; Prissanaroon et al., 2005; Schaefer et al., 2006; Šimor et al., 2003]. The initiation of the ELD process is preceded by a surface activation to provide catalytic sites on the material surface. However, conventional activations require a long process time, intermittent water rinsing and drying, involve the loss of expensive metal ions, and create environmental pollution problems [Touchais-Papet et al., 1999]. Consequently, it is highly desirable to develop simple and more economically and ecologically attractive activations prior to the ELD process [Prissanaroon et al., 2005; Šimor et al., 2003; Touchais-Papet et al., 1999]. Many researchers have investigated methods to advance the activation using laser [Chen et al., 2006], ultraviolet (UV) laser or UV/VUV (vacuum ultraviolet) excimer lamps [Esrom, 2000], plasma [Kreitz et al., 2005], and ion beams [Weller et al., 2003]. However, these techniques require specialized conditions such as vacuum and the coating of palladium (Pd) compounds using spinning-on, spraying, or dip coating [Esrom, 2000; Gray et al., 2005; Kordás et al., 1999]. To improve the catalytic surface activation, recently, Byeon et al. (2007c) reported a strategy for site-selective catalytic surface activation via platinum aerosol nanoparticles for use in silver micropatterning. Aerosol catalysis is shown to be a powerful tool for investigating the catalytic

properties of freshly formed nanoparticles in situ and without substrate interference [Weber et al., 2001].

A strategy for catalytic surface activation by the production of Pd aerosol nanoparticles via spark generation (Figure 37) was introduced. Aerosol activation involves a fewer steps than conventional surface activation, and does not require wet chemical steps. Spark generation has been used to produce the particles of metals, alloys, and compounds for a wide range of materials with particle sizes ranging from several nanometers up to ~100  $\mu\text{m}$  [Watters Jr. et al., 1989]. In this study, spark-generated nanoparticles were captured by ACF due to fibrous filtration [Balazy & Podgórski, 2007]. After thermal curing, the ACF that were catalytically activated by the Pd nanoparticles were immersed in a silver ELD solution to form a silver layer on the activated ACF, and the reduction-oxidation reactions occurred preferentially around the Pd nanoparticles.

### **3.1.2 Site-selective catalytic surface activation via aerosol Pd ELD onto flexible polyimide (FPI) substrate for use in Cu micropatterning**

Copper is an attractive interconnect material for use in high density packaging and ultra-large scale integrated (ULSI) devices since it offers the advantages of low resistivity, high electromigration resistance and high melting point [Zhang et al., 1997]. One of the most widely used techniques for the fabrication of micro- and nano-patterned copper structures on substrates is the electroless deposition (ELD) [Hagberg et al., 2007; Lee et al., 2003; Yanagimoto et al., 2005] of copper, which requires the surface activation of the substrates with a metal catalyst, such as palladium or platinum.

Many researchers have investigated ways to advance the surface activation by combining photochemical [Hozumi et al., 2005], chemical [Khoperia et al., 1997], and self-assembled block copolymer [Sugimura et al., 2001] tools in order to grow site-selective catalysts. Most of these methods are based on photolithographic techniques [Cho et al., 1993; Dressick et al., 1993], recently, methods using laser [Chen et al., 2006; Schrott et al., 1995], ultraviolet (UV) ray [Esrom, 2000], plasma [Kreitz et al., 2005], and ion beams [Weller et al., 2003] have been reported. The use of the above mentioned activation techniques generally involves the deposition of an inorganometallic or organometallic coating. However, there have been some problems reported relating to coating, removal and incomplete decomposition of the precursor [Zhang & Boyd, 1998]. Furthermore, the equipment required to produce laser, UV, plasma, and ion beams are still quite expensive and frequently require a high vacuum environment [Kordás et al., 1999; Zhang & Boyd, 1998].

Other surface activation processes include microcontact printing ( $\mu$ CP) [Geissler et al., 2000; Hendricks & Lee, 2006; Hidber et al., 1996] and inkjet printing (IJP) [Cheng et al., 2005; Shah et al., 1999], these processes create patterned catalyst by directly stamping and jetting the catalyst, respectively. The key step in both  $\mu$ CP and IJP processes is the direct transfer of the catalyst from the stamp or nozzle to the substrate. However, a major challenge in applying a site-selective surface activation using  $\mu$ CP and IJP processes is the formulation of catalyst colloids. Two critical issues with colloids reside in the sedimentation stability of the corresponding colloids, which typically require stabilizers (binders, dispersants and adhesion promoters), and limiting the metal concentration to low values [Busato et al., 2007; Cheng et al., 2005; Shah et al., 1999]. Furthermore, there have also been other problems such as the ability to reproduce the colloidal pattern and the washing of the colloids. To improve the

catalytic activation, recently, [Byeon et al. \(2007c\)](#) reported a strategy for site-selective catalytic activation via platinum aerosol nanoparticles for use in silver micropatterning.

In this paper we introduced a strategy for site-selective catalytic surface activation by production of palladium aerosol nanoparticles via spark generation. Spark generation has been used to produce particles of metals, alloys, and compounds for a wide range of materials having particle sizes ranging from several nanometers up to  $\sim 100\text{ }\mu\text{m}$  [[Schwyn et al., 1988](#); [Watters Jr. et al., 1989](#)]. Our technique does not need any special devices such as laser, UV, plasma, and electron beams, nor does it require special preparations such as catalyst colloid solutions. Furthermore, employing the nanoscale aerosol particles as catalyst caused the effective initiation of ELD due to their large surface area. We enhanced the deposition of palladium aerosol particles onto a substrate by controlling the thermophoresis, which is a physical phenomenon in which aerosol particles [[Gonzalez et al., 2005](#); [Messerer et al., 2003](#); [Zheng, 2002](#)], subjected to a temperature gradient, move from high- to low-temperature zones of the gas.

### **3.1.3 Site-selective catalytic surface activation via aerosol platinum (Pt) ELD onto FPI substrate for use in Ag micropatterning**

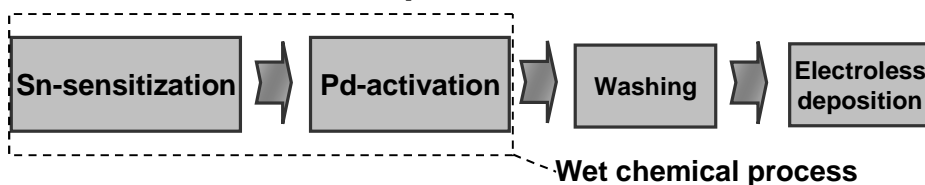
In this section, a strategy for catalytic surface activation by producing platinum aerosol nanoparticles via spark generation was introduced. The deposition of these metal aerosol particles onto a flexible PI substrate was enhanced by controlling the thermophoresis. Without any chemical pretreatment, reproduction of a stable and selective deposition of particles on the PI substrate through a “YONSEI” pattern hole was obtained. After annealing, the catalytically activated PI substrate was immersed in a silver ELD solution that resulted in the ELD of silver on the platinum nanoparticles of the PI substrate.

## **3.2 Materials and Methods**

### **3.2.1 Preparations and characterizations of Pd aerosol activation and Ag ELD onto ACF**

The catalytic surface activation involved the spark generation of Pd aerosol nanoparticles and their filtration by a rayon-based ACF (38 mm in diameter and 2.6 mm in thickness, KF-1600, Toyobo). A spark was generated between two identical Pd rods (diameter: 3 mm, length: 100 mm, Nilaco, Japan) inside a reactor (volume: 42.8 cm<sup>3</sup>) under a pure nitrogen environment (less than 10<sup>-4</sup> impurities) at STP [Byeon et al., 2006]. The flow rate of the nitrogen gas, which was controlled by a mass flow controller, was set to 2 L/min. The electrical circuit specifications were as follows: resistance of 0.5 MΩ; capacitance of 10 nF; loading current of 2 mA; applied voltage of 3 kV; and frequency of 667 Hz. The gas temperature inside the spark channel was increased beyond a critical value [Berkowitz & Walter, 1987], which was sufficient to sublime parts of the electrodes. Since the duration of each spark was very short (~1.5 milliseconds) and the vapors were rapidly cooled after the spark was generated, supersaturation was achieved and the nanoparticles were formed by nucleation/condensation. In order to prevent the detachment of the nanoparticles from the surface of the ACF disc, the disc was separated from the holder and cured in air at 190°C for 5 minutes.

### Conventional “two-step” activation



### Aerosol activation

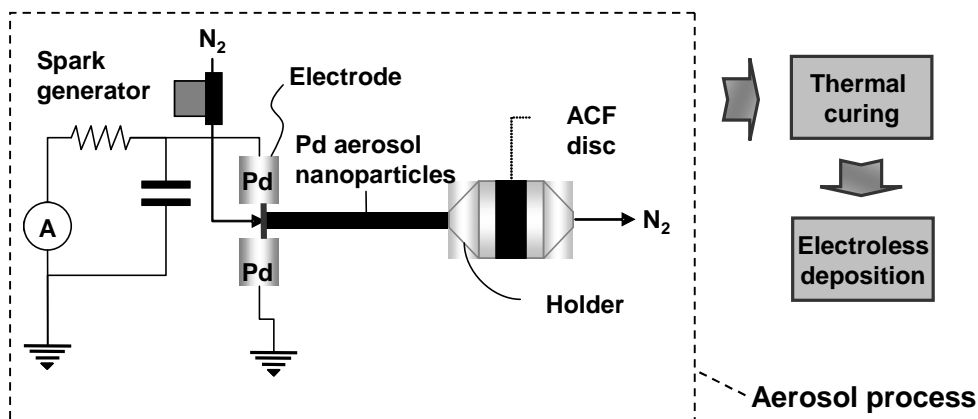


Figure 37. Procedures of conventional and aerosol activation.

For comparison purposes, the surface of another ACF disc was activated by a conventional “two-step” process (Figure 37), which requires sensitization. The ACF disc was first sensitized by immersing it in an aqueous solution containing  $SnCl_2$ ,  $HCl$  (0.05 mL), and deionized (DI) water (49.95 mL) for 2 minutes, followed by rinsing with DI water. The subsequent activation was carried out in a  $PdCl_2$  solution of  $SnCl_2$ ,  $HCl$  (0.05 mL), and DI water (49.95 mL) for 2 minutes, followed by rinsing again with DI water. The amounts of

$\text{SnCl}_2$  and  $\text{PdCl}_2$  in each aqueous solution were varied between 2-36 mg and between 1-18 mg, respectively.

Once an ACF disc was activated by aerosol process or the conventional process, the disc was immersed in a silver ELD solution for the deposition of silver onto the surfaces of the activated ACF disc. Reactions of silver deposition were initiated by the reaction of hydrazine with hydroxide ions producing nitrogen gas and water with a simultaneous release of electrons. The electrons were transferred across the Pd island and used for the decomposition of Ag-amine complexes into Ag metals, generating ammonia gas as a by-product. Nitrogen and ammonia gases evolved as bubbles during the ELD process. After the disc was removed from the ELD solution, it was vigorously rinsed with DI water to remove the residual and then set aside to dry. Two solutions were mixed and used for the ELD solution. Solution A contained 1 g of  $\text{AgNO}_3$ , 60 g of  $\text{Na}_2\text{-EDTA}$ , 88 mL of isopropyl alcohol, 12 mL of acetic acid, and 400 mL of  $\text{NH}_4\text{OH}$  in 1 L of DI water. Solution B contained 3 mL of hydrazine, 2 mL of mercerine, and 400 mL of ethyl alcohol in 1 L of DI water. Fifty milliliters of solution A and thirty milliliters of solution B were mixed together and the activated ACF disc was then immersed into this mixture for 2-30 minutes at  $20^\circ\text{C}$  so that the silver particles would be deposited on the activated ACF disc.

The size distribution of Pd aerosol nanoparticles was measured by a SMPS system. The SMPS system, which measures the mobility equivalent diameter, was operated at a sample flow of 0.3 L/min, sheath flow of 3 L/min, and scan time of 180 seconds (measurement range: 4.61-157 nm). The number concentration of the particles that penetrated through the ACF disc was also measured with the SMPS system. After the particles were sampled on a porous carbon-supported copper grid positioned on a polyamide membrane filter located 20 cm downstream the spark generator, morphologies and microstructures of the Pd nanoparticles

were analyzed using a HRTEM (JEM-3010) operated at 300 kV. X-ray photoelectron spectroscopy (XPS) measurements were performed on a Kratos Axis HIS spectrometer using a monochromatized Al K $\alpha$  X-ray source (1486.6 eV photons) at a constant dwell time of 100 milliseconds and pass energy of 40 eV. The X-ray source was run at a power of 150 W (15 kV and 10 mA). The pressure in the analysis chamber was maintained under 10<sup>-8</sup> Torr during the measurements. All binding energies (BEs) were referenced to the C1s hydrocarbon peak at 284.6 eV. FESEM (JSM-6500F, JEOL, Japan) images and EDX (JED-2300, JEOL, Japan) profiles were obtained at an accelerating voltage of 15 kV. The amount of silver particles deposited on the ACF disc was determined by ICP-AES (Elan 6000, Perkin-Elmer, US). Approximately 0.1 g of the sample was dissolved in 50 mL nitric acid, and the mixture was diluted to 100 mL with DI water. After 3 h, the sample was filtered out and a part of the remaining mixture was delivered in a volumetric flask for ICP-AES analyses. XRD studies of the silver particles were carried out on a Rigaku RINT-2100 diffractometer equipped with a thin-film attachment using Cu-K $\alpha$  radiation (40 kV, 40 mA). The 2 $\theta$  angles ranged from 10 to 90° at 4°/min by step scanning at an interval of 0.08°. The crystallite size of silver was calculated from the XRD spectra in accordance with Scherrer's formula ( $t = 0.9\lambda / (B \cos \theta)$ ). Nitrogen adsorption isotherms of the ACF samples were measured using a porosimeter (ASAP 2010, Micromeritics Ins. Corp., US) at 77.4 K with relative pressure ranging from 10<sup>-6</sup> to 1.

### **3.2.2 Preparations and characterizations of site-selective Pd aerosol activation and Cu ELD onto FPI**

Figure 38 shows an overview of our aerosol activation. The palladium aerosol nanoparticles were generated via spark discharge and carried by N<sub>2</sub> gas to a PI substrate



through a hole in pattern mask (150  $\mu\text{m}$  width x 100  $\mu\text{m}$  depth for line pattern, 400  $\mu\text{m}$  width x 400  $\mu\text{m}$  length x 100  $\mu\text{m}$  depth for square pattern) for a duration of 15 minutes. In the experiments, commercially available PI films (Kapton<sup>TM</sup>, Dupont) having a 50  $\mu\text{m}$  thickness were used as the substrates. A spark was generated between two identical palladium rods (diameter: 3 mm, length: 100 mm) inside a reactor (volume: 42.8  $\text{cm}^3$ ) under a pure nitrogen environment (less than  $10^{-4}$  impurities) at STP [Byeon et al., 2006]. The flow rate of the nitrogen gas, which was controlled by a mass flow controller, was set at 60 mL/min. The electrical circuit specifications were as follows: resistance of 0.5  $\text{M}\Omega$ , capacitance of 10 nF, loading current of 2 mA, applied voltage of 2.8 kV, and frequency of 667 Hz. The spark channel raised the gas temperature within the channel above a critical value [Berkowitz & Walter, 1987], which is enough to sublime part of the electrodes. Since the duration of each spark was very short (~1.5 milliseconds) and the vapors were rapidly cooled after the spark, supersaturation was achieved and nanoparticles were formed by nucleation/condensation.

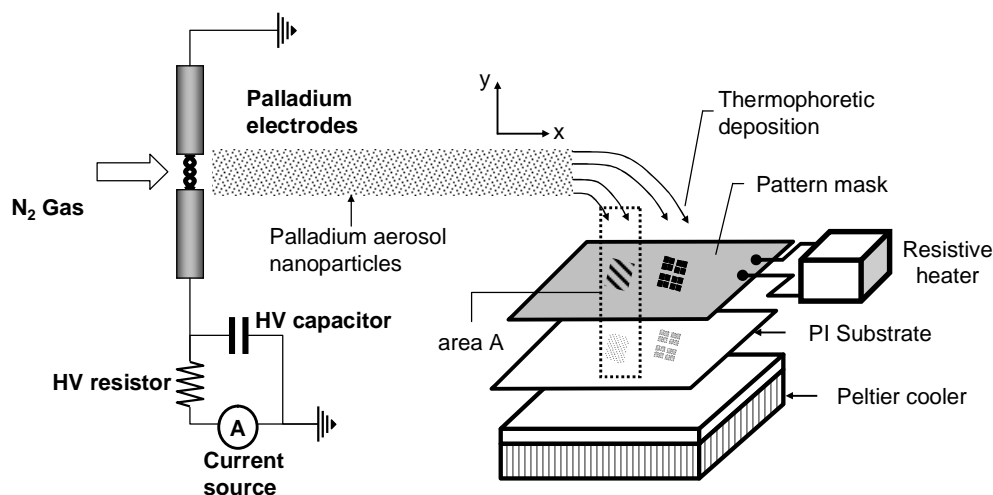


Figure 38. Overview of site-selective aerosol activation.

While the temperature of the particle-laden flow was kept at 20°C, the temperatures of the stainless steel mask and PI substrate were kept at 22°C (for preventing unwanted deposition of the particles onto the mask via thermophoresis) and 4°C (for enhancing the deposition of the particles onto the PI substrate via thermophoresis) through the use of a resistive heater and a Peltier cooler, respectively. The PI substrate was then separated from the mask and annealed at 190 °C for 5 minutes in air to prevent detachment of the particles from the PI substrate. After annealing, the catalytically activated PI substrate was immersed into a copper ELD solution that resulted in the ELD of copper on the palladium nanoparticles of the PI substrate. The ELD of copper at 20°C resulted in copper patterns appearing within 40 minutes. The schematic of copper ELD onto the line and square palladium patterns is shown in Figure 39. The overall reactions are also described in Figure 39. Two solutions were mixed and used for the ELD solution. Solution A contained 3 g of CuSO<sub>4</sub>, 14 g of sodium potassium tartrate (Rochelle salt), and 4 g of NaOH in 100 mL of deionized water. Solution B was an aqueous formaldehyde solution (37.2 wt%). The two solutions A and B were mixed in a 10:1 (v/v) ratio and the activated PI substrate then immersed into the mixture so that copper particles would be coated on the activated sites. The PI substrate was rinsed with deionized water after it was removed from the ELD solution to remove the residual and then set aside to dry.

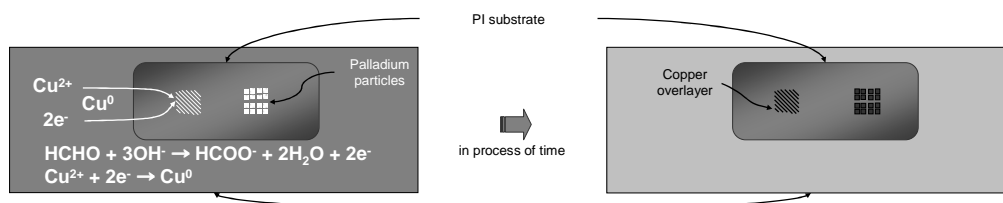


Figure 39. Schematic of copper ELD onto the line and square palladium patterns.

The size distribution of aerosol nanoparticles was measured by a SMPS system consisting of an electrostatic classifier (TSI 3081), a condensation particle counter (TSI 3025), and an aerosol charge neutralizer. The SMPS system was operated with a sample flow 0.3 L/min, a sheath flow of 3 L/min, and a scan time of 180 seconds (measurement range between 13.8-723 nm). After the particles were sampled on a porous carbon-supported copper grid located on a polyamide membrane filter 20 cm downstream of the spark generator, morphologies of the particles were analyzed using a high resolution transmission electron microscope (HRTEM, JEM-3010) operated at 300 kV. Field emission scanning electron microscope (FESEM, JSM-6500F, JEOL, Japan) images and energy dispersive X-ray (EDX, JED-2300, JEOL, Japan) profiles were obtained at an accelerating voltage of 15 kV. X-ray photoelectron spectroscopy (XPS) measurements were performed on a Kratos AXIS HIS spectrometer using a monochromatized Al K $\alpha$  X-ray source (1486.6 eV photons) at a constant dwell time of 100 milliseconds and pass energy of 40 eV. The X-ray source was run at a power of 150 W (15 kV and 10 mA). The pressure in the analysis chamber was maintained under  $10^{-8}$  Torr during the measurements. All binding energies (BEs) were referenced to the C1s hydrocarbon peak at 284.6 eV. X-ray diffraction (XRD) studies of the copper patterns were carried out on a Rigaku RINT-2100 diffractometer equipped with a thin film attachment using Cu-K $\alpha$  radiation (40 kV, 40 mA). The  $2\theta$  angles ranged between 10 to 90° with 4°/min by step scanning at an interval of 0.08°. The crystallite size of copper was calculated from the XRD spectra in accordance with Scherrer's formula ( $t=0.9\lambda/(B\cos\theta)$ ). An atomic force microscope (AFM) was used for the topography of the patterns. Topographic images were recorded under ambient conditions using a multimode scanning probe microscope (SPM) connected to a

NanoScope IIIa controller. For the high-resolution images an E-scanner having a maximum scanning size of 125  $\mu\text{m}$  and a resolution of 0.2  $\text{\AA}$  was used. The SPM was operated in tapping mode, which allowed topography and phase contrast images to be recorded. The drive frequency was 330 kHz, and the voltage was between 3.0 and 4.0 V. The drive amplitude was about 300 mV, and the scan rate was 0.5-1.0Hz. An arithmetic mean of the surface roughness was calculated from the roughness profile determined by SPM. Resistances of the patterns were measured using a 4-point probe (CMT-SR200N, Changmin Co., Ltd., Korea). Resistivities were calculated from the resistances and the thicknesses of the patterns that were obtained by AFM observation. I-V measurements were performed in air using an Agilent 5263A source-measure unit.

### **3.2.3 Preparations and characterizations of site-selective Pt aerosol activation and Ag ELD onto FPI**

Figure 55(a) shows an overview of aerosol activation. The platinum nanoparticles were generated via spark discharge and carried by  $\text{N}_2$  gas to a PI substrate through the pattern hole (width: 100  $\mu\text{m}$ , depth: 100  $\mu\text{m}$ ) of the “YONSEI” mask for a duration of 5 minutes. In the experiments, commercially available PI films (Kapton<sup>TM</sup>, Dupont) having a 50  $\mu\text{m}$  thickness were used as the substrates. While the temperature of the particle-laden flow was kept at 20°C, the temperatures of the stainless steel mask and PI substrate were kept at 22°C (for preventing unwanted deposition of the particles onto the mask via thermophoresis) and 4°C (for enhancing the deposition of the particles onto the PI substrate via thermophoresis) through the use of a resistive heater and a Peltier cooler, respectively. As shown in Figure 55(a), the particles were

selectively deposited on the PI substrate by thermophoresis ([Supplementary Data 4](#)) due to the temperature distribution inside the dotted area A (Figure 55(b)).

A spark was generated between two identical platinum rods (diameter: 3mm; length: 100mm) inside a reactor (volume: 42.8 cm<sup>3</sup>) under a pure nitrogen environment (less than 10<sup>-4</sup> impurities) at STP [[Byeon et al., 2006](#)]. The flow rate of the nitrogen gas, which was controlled by a mass flow controller, was set at 100 mL/min. The electrical circuit specifications were as follows: resistance of 0.5 MΩ; capacitance of 10nF; loading current of 2 mA; applied voltage of 2.8 kV; and frequency of 667 Hz. The spark channel raised the gas temperature within the channel above a critical value [[Berkowitz & Walter, 1987](#)], which is enough to sublime part of the electrodes. Since the duration of each spark was very short (~1.5 milliseconds) and the vapors were rapidly cooled after the spark, supersaturation was achieved and nanoparticles were formed by nucleation/condensation.

Solution A contained 2 g of AgNO<sub>3</sub>, 60 g of Na<sub>2</sub>-EDTA, 88mL of isopropyl alcohol, 12 mL of acetic acid and 400 mL of NH<sub>4</sub>OH in 1L of deionized water. Solution B contained 3mL of hydrazine, 2 mL of mercerine and 400 mL of ethyl alcohol in 1 L of deionized water. 30 mL of Solution A and 30 mL of Solution B were mixed together and the activated PI substrate was then immersed into the mixture for 10 minutes at 20°C so that silver particles would be coated on the activated substrate.

### **3.3 Results and discussion**

#### **3.3.1 Properties of Pd aerosol activation and Ag ELD onto ACF**

Figure 40 shows the size distribution of spark generated aerosol nanoparticles measured using the SMPS system. The geometric mean diameter and geometric standard

deviation were 25.5 nm and 1.54, respectively. The total number concentration was  $8.8 \times 10^6$  particles/cm<sup>3</sup>. Figure 40 also shows the fractional (grade) collection efficiency of an ACF disc as a function of particle size. The efficiency is defined by

$$\eta_{ACF}(d_p) = 1 - [C_{ACF}(d_p)/C_0(d_p)] \quad (4)$$

where  $C_0(d_p)$  is the freestream concentration of the particles and  $C_{ACF}(d_p)$  is the concentration after filtration by the ACF disc. The morphology and structure of the nanoparticles were characterized by the HRTEM and XPS, respectively. The HRTEM micrograph (Figure 41) shows that the nanoparticles were agglomerates of primary particles (each ~28 Å in diameter). The XPS profile (Figure 42) of the nanoparticles reveals that they were pure Pd. The BE doublets with the BEs of the Pd 3d<sub>5/2</sub> and Pd 3d<sub>3/2</sub> peak components located at approximately 335 and 340 eV, respectively, are assigned to the Pd<sup>0</sup> species [Persson et al., 2007]. Figure 43 shows SEM micrographs of conventionally activated and aerosol activated ACF samples. While a pristine ACF disc had a clean surface, in any activation, more number of particles were deposited on the ACF by increasing the activation intensity from 0.23 to 4.25 mg-Pd/g-ACF. From the EDX analyses (Figure 44), it was found that the pristine sample contained carbon and oxygen, which may have originated from the ACF, while any activated sample contained a small amount of Pd. The conventionally activated sample also contained a small amount of tin and chlorine, which may have originated from tin sensitization and Pd activation.

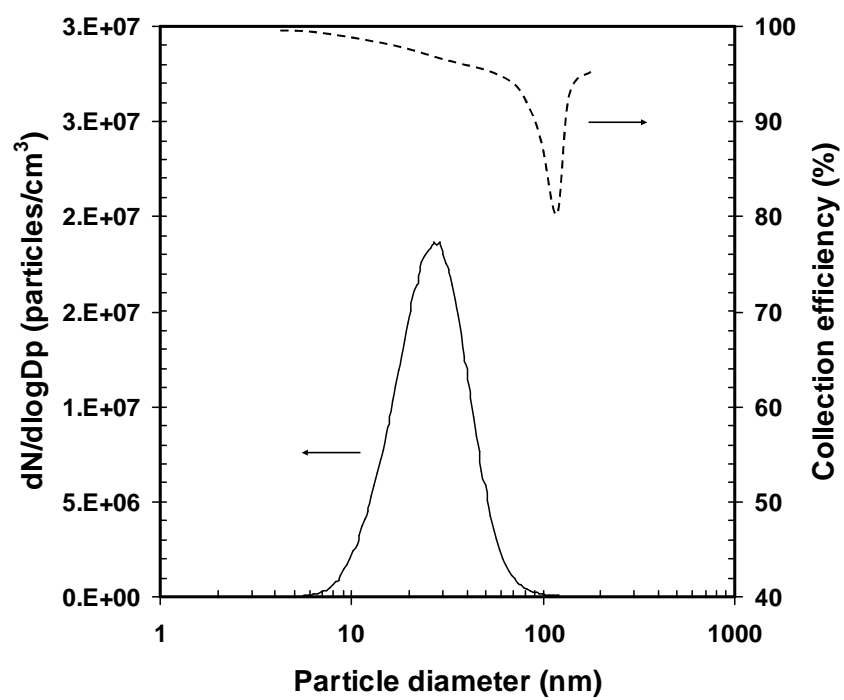


Figure 40. Particle size distribution of spark generated aerosol nanoparticles and collection efficiency of ACF.

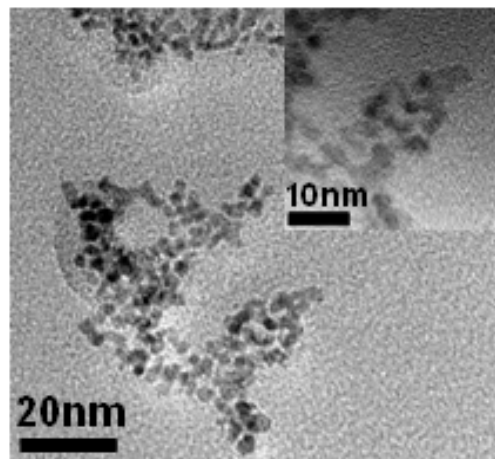


Figure 41. HRTEM micrograph of spark generated nanoparticles.

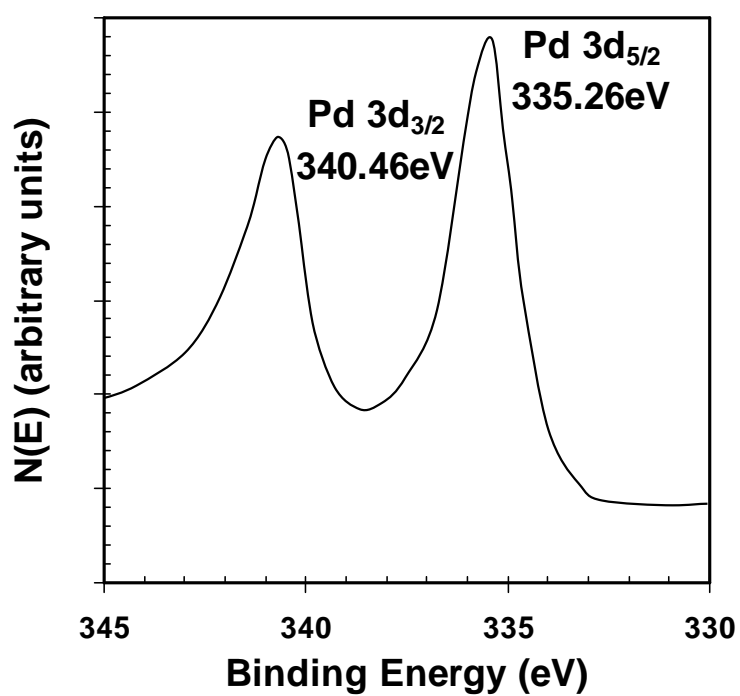


Figure 42. XPS profile of spark generated aerosol nanoparticles.

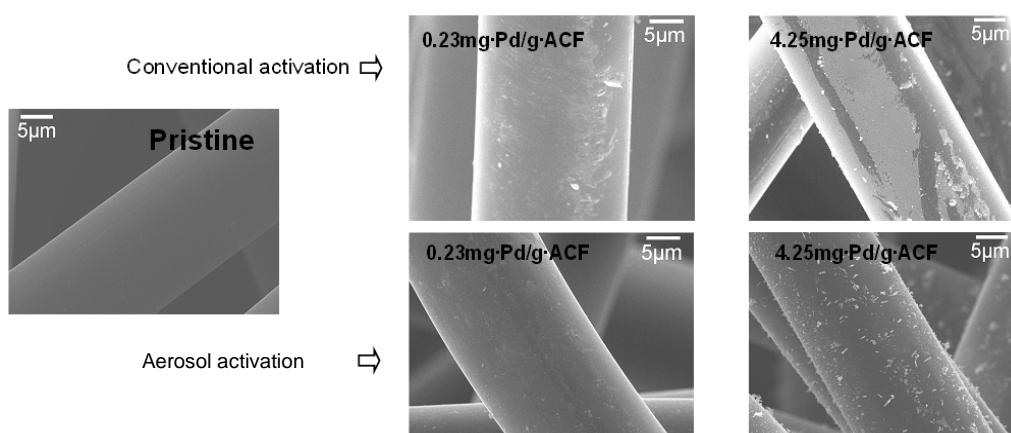




Figure 43. SEM micrographs of conventionally and aerosol activated ACF.

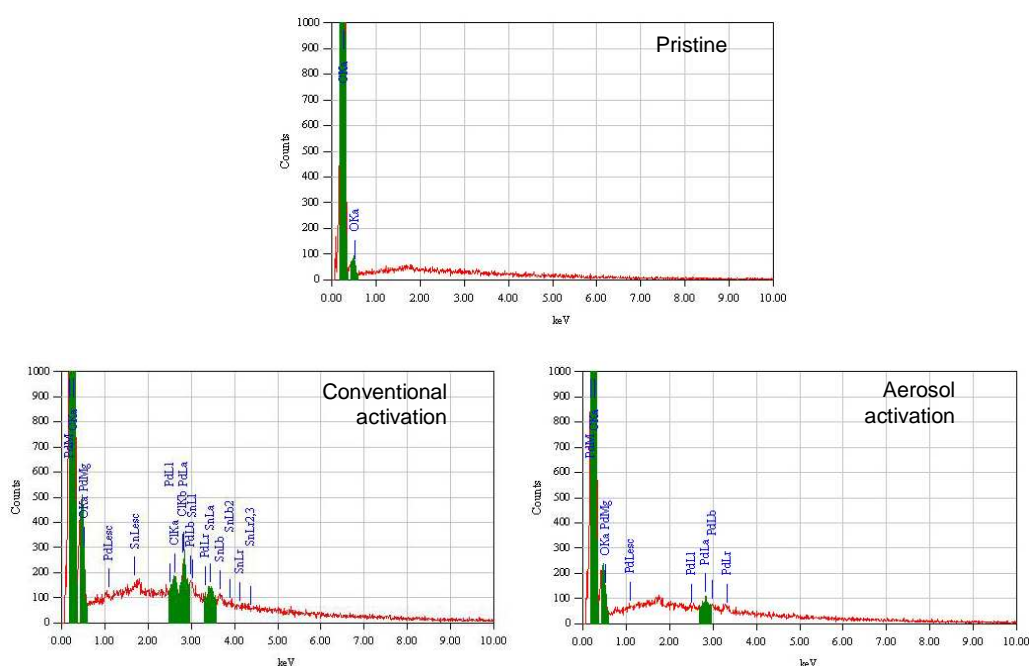
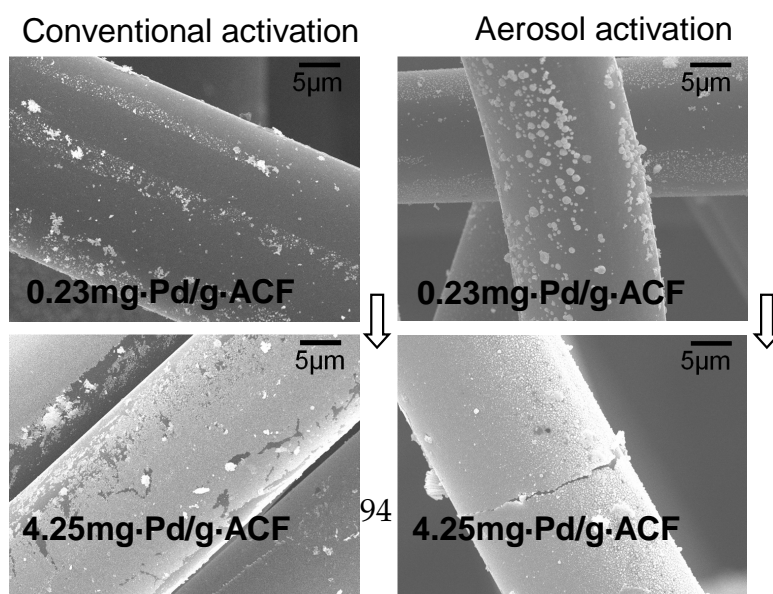



Figure 44. EDX profiles of conventionally and aerosol activated ACF.

Figure 45 shows that particles on the ACF were subsequently formed after the ELD process. The SEM micrographs of conventional and aerosol activations were obtained by varying the activation intensity obtained after ELD for 10 minutes. The amount of particles was proportional to the activation intensity. Figure 46 shows the trend of particle deposition on an aerosol activated ACF disc with ELD time at an activation intensity of 1.42 mg-Pd/g-ACF.

From the EDX analyses (Figure 47), it was found that the coated metal was mainly comprised of silver; however, it contained a small amount of Pd. Carbon and oxygen, which may have originated from the ACF, were also detected. For the conventionally activated ACF, tin and chlorine were detected in addition to silver, Pd, carbon, and oxygen. Figure 48 summarizes the plots of mass of silver deposited onto the ACF as a function of activation intensity (for an ELD time of 10 minutes) and ELD time (at an activation intensity of 1.42 mg-Pd/g-ACF). The results were obtained from the ICP-AES analyses. The mass increased with time due to a continuous reduction in silver ions on previously deposited silver particles (autocatalytic process) [Gray et al., 2005; Schaefers et al., 2006]. The XRD profiles (Figure 49) of the silver particles show that there exist four peaks located at  $2\theta = 38.2, 44.4, 54.5,$  and  $77.5^\circ$ . A comparison of these peaks with the data from powder diffraction file no. 01-0783 reveals that these peaks correspond to the [111], [200], [220], and [311] planes of the face-centered cubic phase of silver. The data imply the characteristics of pure metallic silver with good crystallinity and without any impurity phase. The intensities of the silver peaks increased with increasing ELD time (or activation intensity), which was caused by the growth of the silver particles. The average crystal sizes were evaluated according to Scherrer's formula and the results are shown in Table 10. It was found that the size was proportional to either activation intensity or ELD time.





Two SEM images of a fiber are shown side-by-side, separated by a right-pointing arrow. The left image is labeled '2min' and shows a fiber with a rough, irregular surface. The right image is labeled '30min' and shows a fiber with a much smoother surface. Both images include a 5 μm scale bar in the top right corner.

Figure 47. EDX profiles of particle deposited ACF (10 min of ELD, 1.42 mg·Pd/g·ACF).

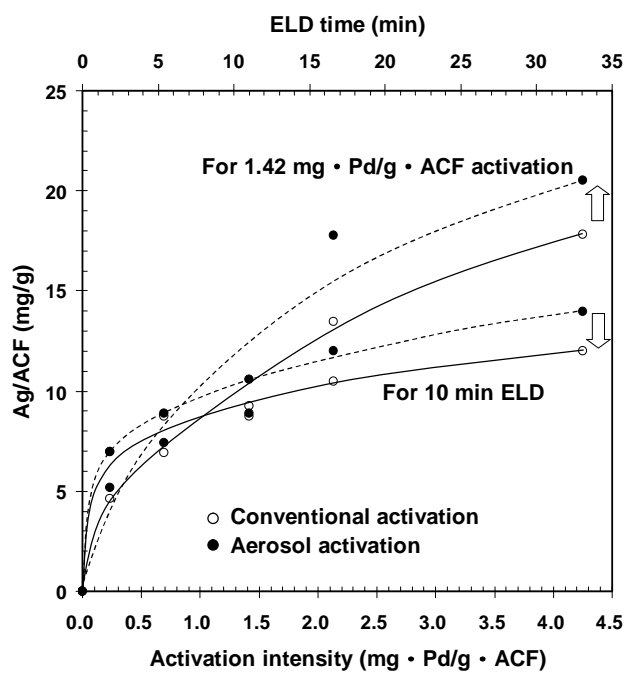


Figure 48. Results of ICP-AES analyses of silver deposited ACF.

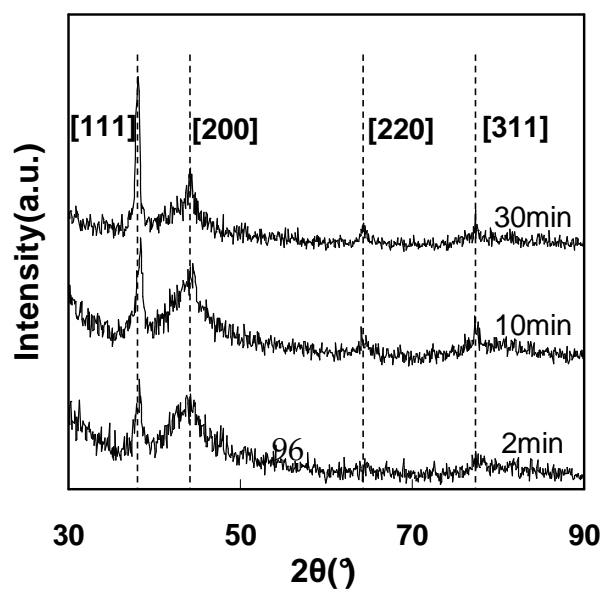


Figure 49. Results of XRD analyses of silver deposited ACF.

Table 10 Crystal sizes (nm) of silver particles vs activation intensity and ELD time

ELD	Activation intensity (mg·Pd/g·ACF)							
time	0.23		0.69		1.42		4.25	
(min)	CA	AA	CA	AA	CA	AA	CA	AA
2	2.21	3.48	7.01	10.78	12.04	13.89	26.63	28.84
5	3.55	4.21	9.33	10.02	17.12	19.51	31.11	32.89
10	4.22	4.93	11.36	12.02	20.33	22.65	35.14	38.79
18	5.01	5.28	14.88	15.68	23.25	26.01	39.18	41.24
30	5.66	6.13	16.16	16.81	31.05	33.25	46.13	48.21

CA: Conventional activation

AA: Aerosol activation

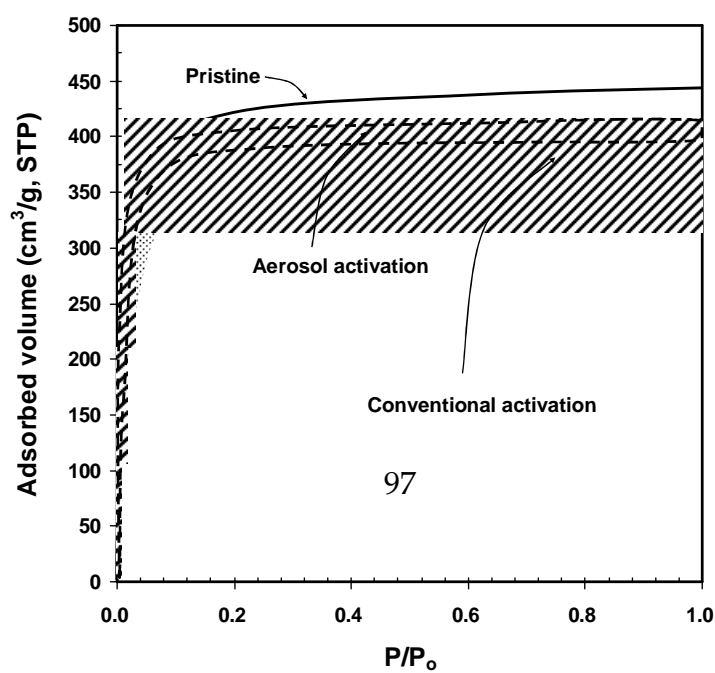


Figure 50. Adsorption isotherms of silver deposited ACF.

Table 11 Textural properties of silver deposited ACF vs activation intensity and ELD time

ELD time (min)	Activation intensity (mg-Pd/g-ACF)			
	0.23		4.25	
	TSSA (m <sup>2</sup> /g) / MSSA (m <sup>2</sup> /g) / TPV (cm <sup>3</sup> /g) / MPV (cm <sup>3</sup> /g) / APD (Å) (1610/ 1593/ 0.87/ 0.85/ 17.7 for pristine)			
	CA	AA	CA	AA
2	1399/1226/0.72/0.70/17.0	1532/1488/0.80/0.78/17.5	1277/1202/0.65/0.64/16.8	1359/1325/0.72/0.70/17.1
10	1242/1206/0.69/0.67/16.5	1382/1358/0.77/0.76/17.2	1104/1072/0.60/0.57/16.3	1286/1225/0.67/0.65/16.9
30	1091/1003/0.65/0.62/15.9	1284/1236/0.69/0.67/16.6	912/803/0.52/0.51/15.4	1201/1056/0.61/0.59/16.1

Figure 50 shows that a major uptake occurred at a relatively low pressure ( $P/P_o < 1$ ) and a plateau was attained at  $P/P_o \approx 0.3$ , implying that all the ACF samples had microporous characteristics (type I isotherm) according to the IUPAC classification [Brunauer et al., 1938]. The specific surface area of the pristine ACF was the largest; however, it decreased as the amount of deposited silver increased since the deposited silver particles could block or occupy some pores of the pristine ACF. Detailed results of the textural properties of the samples are summarized in Table 11. When either the activation intensity or ELD time was increased in aerosol activation, the decrease in the specific surface areas, pore volumes, and average pore diameters was less than that in the conventional activation.